Review

Recent progress in research on tungsten materials for nuclear fusion applications in Europe

M. Rieth [a,*], S.L. Dudarev [b], S.M. Gonzalez de Vicente [c], J. Aktaa [a], T. Ahlgren [s], S. Antusch [a], D.E.J. Armstrong [ab], M. Balden [p], N. Baluc [o], M.-F. Barthe [q,r], W.W. Basuki [a], M. Battabyal [o], C.S. Becquart [t], D. Blagoeva [i], H. Boldyryeva [h], J. Brinkmann [p], M. Celino [k], L. Ciupinski [e], J.B. Correia [m], A. De Backer [t], C. Domain [x], E. Gaganidze [a], C. García-Rosales [n], J. Gibson [ab], M.R. Gilbert [b], S. Giusepponi [k], B. Gludovatz [j], H. Greuner [p], K. Heinola [s], T. Höschen [p], A. Hoffmann [z], N. Holstein [a], F. Koch [p], W. Krauss [a], H. Li [j], S. Lindig [p], J. Linke [d], Ch. Linsmeier [p], P. López-Ruiz [n], H. Maier [p], J. Matejicek [h], T.P. Mishra [p], M. Muhammed [l], A. Muñoz [f], M. Muzyk [e], K. Nordlund [s], D. Nguyen-Manh [b], J. Opschoor [w], N. Ordás [n], T. Palacios [y], G. Pintsuk [d], R. Pippan [j], J. Reiser [a], J. Riesch [p], S.G. Roberts [ab], L. Romaner [ac], M. Rosiński [e], M. Sanchez [g], W. Schulmeyer [z], H. Traxler [z], A. Ureña [g], J.G. van der Laan [aa], L. Veleva [o], S. Wahlberg [l], M. Walter [a], T. Weber [a], T. Weitkamp [u,v], S. Wurster [j], M.A. Yar [l], J.H. You [p], A. Zivelonghi [p]

[a] Karlsruhe Institute of Technology, Institute for Applied Materials, Karlsruhe, Germany
[b] EURATOM/CCFE Fusion Association, Culham Science Centre, Abingdon OX14 3DB, UK
[c] EFDA-Close Support Unit, Garching, Germany
[d] Forschungszentrum Jülich, EURATOM Association, Germany
[e] Faculty of Materials Science and Engineering, Warsaw University of Technology, Woloska 141, 02-507 Warsaw, Poland
[f] Departamento de Física, Universidad Carlos III, Avda. de la Universidad 30, 28911 Leganés, Madrid, Spain
[g] Departamento de Ciencia e Ingeniería de Materiales, ESCET, Universidad Rey Juan Carlos, C/Tulipán s/n 28933 Móstoles, Madrid, Spain
[h] Institute of Plasma Physics, Za Slovankou 3, 18200 Praha, Czech Republic
[i] NRG, Nuclear Research & consultancy Group, Petten, The Netherlands
[j] ÖAW, Erich Schmid Institute of Materials Science, Leoben, Austria
[k] ENEA, C.R. Casaccia, Via Anguillarese 301, 00123 Rome, Italy
[l] KTH, Department of Functional Materials, Stockholm, Sweden
[m] Association EURATOM-IST, Instituto de Plasmas e Fusão Nuclear-Laboratório Associado, Instituto Superior Técnico, Universidade Técnica de Lisboa, Portugal
[n] CEIT and Tecnun (University of Navarra), Paseo de Manuel Lardizabal15, 20018 San Sebastian, Spain
[o] Centre de Recherches en Physique des Plasmas, CRPP EPFL - Materials, 5232 Villigen/PSI, Switzerland
[p] Max-Planck-Institut für Plasmaphysik, EURATOM Association, Garching, Germany
[q] CNRS, UPR3079 CEMHTI, 1D Avenue, de la Recherche Scientifique, 45071 Orléans cedex 2, France
[r] Université d'Orléans, Polytech ou Faculté des Sciences, Avenue du Parc Floral, BP 6749, 45067 Orléans cedex 2, France
[s] University of Helsinki, Department of Physics, Helsinki, Finland
[t] Unité Matériaux et Transformations, UMR 8207, 59655 Villeneuve d'Ascq, France
[u] ESRF Grenoble, 6 Rue Jules Horowitz, 38043 Grenoble, France
[v] Synchrotron Soleil, L'Orme des Merisiers, St Aubin, 91190 Gif-sur-Yvette, France
[w] ECN, Energy Research Centre of the Netherlands, Petten, The Netherlands
[x] EDF R&D, Les Renardières, 77250 Moret sur Loing, France
[y] Universidad Politécnica de Madrid, Materials Science Department, Madrid, Spain
[z] PLANSEE SE, Metallwerk-Plansee-Straße 71, 6600 Reutte, Austria
[aa] Consultant, 1831 AD 25, The Netherlands
[ab] Department of Materials, University of Oxford, UK
[ac] Atomistic Modelling and Design of Materials, Montanuniversität Leoben, Franz-Josef-Straße 18, A-8700 Leoben, Austria

A R T I C L E   I N F O

A B S T R A C T

The current magnetic confinement nuclear fusion power reactor concepts going beyond ITER are based on assumptions about the availability of materials with extreme mechanical, heat, and neutron load capacity. In Europe, the development of such structural and armour materials together with the necessary production, machining, and fabrication technologies is pursued within the EFDA long-term fusion

* Corresponding author. Address: Karlsruhe Institute of Technology – Campus Nord, Institute for Applied Materials, P.O. Box 3640, 76021 Karlsruhe, Germany. Tel.: +49 721 6082 2909; fax: +49 721 6082 4567.
    E-mail address: Michael.rieth@kit.edu (M. Rieth).

materials programme. This paper reviews the progress of work within the programme in the area of tungsten and tungsten alloys. Results, conclusions, and future projections are summarized for each of the programme's main subtopics, which are: (1) fabrication, (2) structural W materials, (3) W armour materials, and (4) materials science and modelling. It gives a detailed overview of the latest results on materials research, fabrication processes, joining options, high heat flux testing, plasticity studies, modelling, and validation experiments.

Contents

1. Introduction

The use of tungsten and tungsten alloys for the helium-cooled divertor and possibly for the protection of the helium-cooled first wall in reactor designs going beyond ITER has been discussed and investigated for several years (see, for example, [1–8]). The structure of the Tungsten and Tungsten Alloys (W&WALLOYS) programme of the EFDA Topical Group on Fusion Materials can be found in [9], which also gives a comprehensive review of activities. The main objective is still to develop and demonstrate the possible applications, as well as to identify limitations to the use of tungsten and tungsten-based materials in future fusion reactors. These will certainly differ significantly from those used in ITER in that they will encounter much higher neutron irradiation dose and nuclear transmutation rates. But even neglecting the irradiation effects (due to the large gaps in the knowledge of properties of these materials), there are still unsolved problems related to the use and properties of tungsten materials.

Like ITER, the future demonstration fusion reactor (DEMO) will be a so-called tokamak in which the plasma is magnetically confined within a torus-shaped vacuum vessel. Fig. 1 shows a typical cross-section of the torus. The major part of the inner surface is covered by blanket boxes in which about 85% of the fusion power is converted and in which lithium has to be transmuted into tritium. The plasma facing surface of these blanket boxes is called the "first wall" (labelled 1 in Fig. 1). Under normal operating conditions its heat load will be around 2 MW/m² and in helium cooled designs ferritic–martensitic 9% Cr steels are the candidate for structural materials. However, there could be off-normal events in which the plasma could damage the first wall. Therefore, a protection layer consisting of tungsten or of a tungsten alloy might be an option. In this paper, such materials are referred to as armour materials.

To make a continuous operation possible, the plasma has to be cleaned from hydrogen isotopes, helium (the "exhaustgas" of nuclear fusion) and from impurities (such as particles of the first wall) which are unavoidable. These ions are redirected from the burning plasma by magnetic fields towards cooled target plates (labelled 2 and 3 in Fig. 1), the so-called divertors. During their impact (or briefly before), the ions recombine to neutral atoms which can then be removed by vacuum pumps. Due to the particle impact, the target plates suffer extraordinarily from sputtering (of a few millimeters during the lifetime). Furthermore, the divertors are the highest thermally loaded components of a fusion power plant. About 15% of the total fusion power has to be removed by divertors while peak loads of 10–20 MW/m² have to be considered. Like the protection layer of the first wall, the plasma facing divertor parts are intended to be made of tungsten or tungsten alloys. In helium cooled divertor designs tungsten materials are also considered for structural use (e.g. as pressurized pipes or thimbles). Since the requirements for both applications (armour or structure) are quite different, in this paper we distinguish between armour and structural materials which in both cases could be tungsten.

In addition, all plasma facing components are exposed to fast neutrons. That is, damage, wear, and aging can reduce the durability of some divertor components significantly. Therefore, divertors have to have a modular design for an easy exchange of these parts. That is why current R&D programmes focus on the development of high-performance materials as well as on design-studies of divertor modules.

Of course, the in-service temperature of the involved parts is a major design criterion and depends strongly on the underlying cooling concept (e.g. water or gas). Thermal load capacity, heat conductivity, or recrystallization, however, are typical properties which restrict the design significantly on the upper temperature limit while brittleness and irradiation damage narrow the structural materials of question on the low-temperature range. Moreover, specific defect processes such as helium bubbles, swelling, new kind of surface reactions, crack formation, or tritium retention considerations have to be considered for the use of armour materials and for the application of possible coatings and protection layers.

In what follows, the results, conclusions, and outlooks are summarized for each of the W&WALLOYS programme's main subtopics, which are (1) fabrication, (2) structural W materials, (3) W armour materials, and (4) materials science and modelling.

Note: Throughout this paper, if not explicitly mentioned otherwise, all chemical compositions are given in weight percent (wt.%).
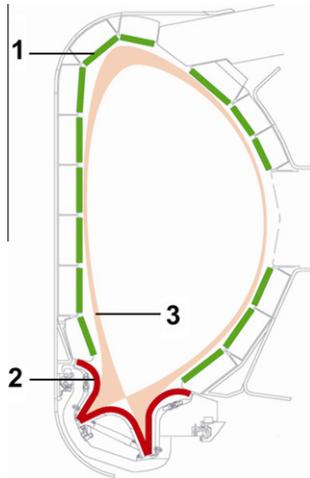
Fig. 1. The illustration shows the cross-section of the torus of a tokamak. (1) The plasma-facing part of the blanket boxes – the so-called first wall. (2) The high heat flux cooling layout of the divertor. (3) The magnetic field lines which direct exhaust particles (mainly helium) to the divertor target plates.
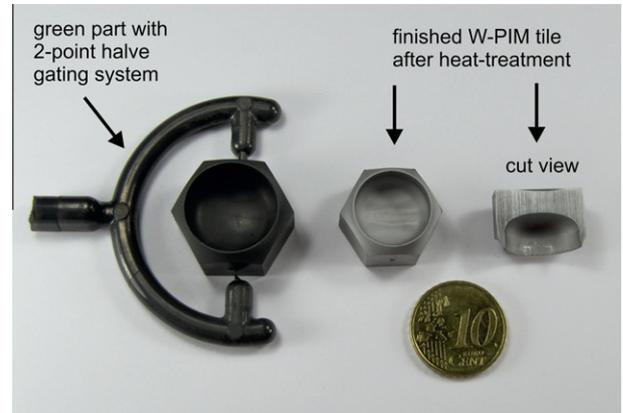

Fig. 3. Powder injection moulding (PIM) of tungsten armour tiles. Green part with gating system (left) and finished parts after heat-treatment (middle + right).
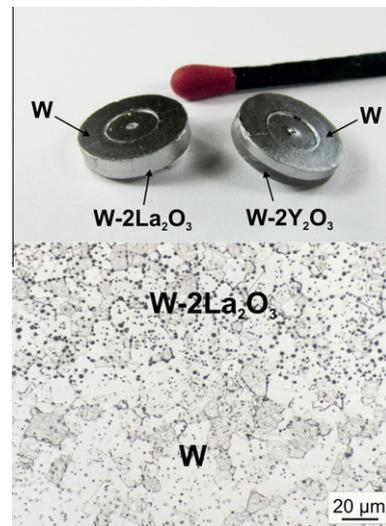

Fig. 4. Upper image: Inlay-two-component W-PIM of discs (W and W–2%La$_2$O$_3$ as well as W and W–2%Y$_2$O$_3$). Lower image: SEM image of the cross-section of the W–2%La$_2$O$_3$ disc.

2. Fabrication

The helium-cooled finger design [3] has so far been used as a reference for component fabrication issues. The most important questions in this field are: What mass fabrication methods can be applied for the thimbles and possibly for the tiles? Are there feasible processes for W–W and W–steel joints?

2.1. Fabrication process development

Due to its unfavourable grain orientation, rod material cannot be used to machine a thimble by turning or milling. The most promising machining route consists of deep drawing of a W plate, which results in grains that follow the contour. It can be taken as given that for components made of tungsten 'grain boundary alignment' is a highly necessary tool in order to create the best possible arrangement for external forces acting on the weak grain boundaries. Therefore, it would be necessary to deep draw a thimble from a 1 mm tungsten plate. Consequently, the tungsten plate material which has been chosen for deep drawing is unalloyed 99.97% pure tungsten (standard rolled commercial grade) with a thickness of

1 mm. This commercially available material was produced by PLANSEE SE, Reutte/Austria. In a deep drawing tool, tungsten blanks with diameters of 23 mm and 26 mm were deep drawn
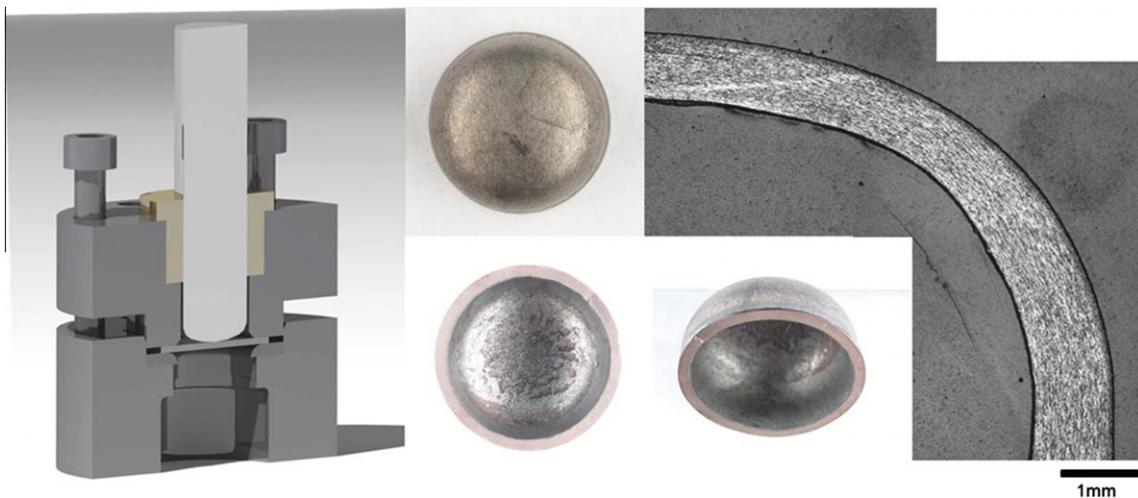

Fig. 2. Deep drawing tool, the results with a blank of 26 mm in diameter, and a micrograph of the cross-section.

successfully in vacuum (about 10^{-5} mbar) at 600 °C with a strain rate of 0.1 mm/min. In Fig. 2 the deep drawing tool, the results with a blank of 26 mm in diameter, and a micrograph which demonstrates that the grains follow the contour of the thimble are shown. For more details on the deep drawing assessment see [10].

Powder injection moulding (PIM) was investigated as a mass fabrication option for the tungsten armour tiles which had to be joined to the thimbles. A new tool design enabled the first production of such tiles (see Fig. 3) via PIM (pre-sintering at 1600 °C for 2 h in H_2 atmosphere followed by a HIP cycle with 250 MPa at 1650 °C for 3 h in Ar atmosphere). With that, the final parts showed 98.6–99% of the theoretical density, Vickers hardness of 457 HV0.1, and a grain size of approximately 5 μm [11].

According to the design, the tiles (pure tungsten) and the mechanical machined thimbles (WL10) have to be joined together by brazing which would have several drawbacks and would also be time intensive. As a mass production alternative, two-component tungsten PIM was investigated using different pure and alloyed W powders. It would allow the joining of two different materials in one process – in this case tungsten and tungsten-ODS alloys. Fig. 4 shows the result of first preliminary tests via insert-two-component W-PIM. This is a two-step process to produce one part. The compositions of the finished discs after heat-treatment (pre-sintering at 1800 °C, 2 h, H_2 and HIP at 2100 °C, 3 h, 250 MPa, Ar atmosphere) are W and W–2 wt.%La_2O_3 as well as W and W–2wt.%Y_2O_3. The cross-section of the finished W–2%La_2O_3 disc is also shown in Fig. 4. There are neither no cracks or voids in the joining zone, which is encouraging for further investigations.

2.2. Joining and transitions from steel to tungsten

One result of the investigations for using electrochemistry for brazing layers fabrication is that the brazing material can be built up from a sequence of electrochemically deposited layers. Growing of galvanic layers from suitable low temperature liquid electrolytes depends on the transported charge and thus can easily be controlled over a wide range by current flow and/or deposition time. Typical elements which can be used for joining may range from Ti, V via Ni, Fe up to Pd and Cu. Further, interlayers with an active functionality which interact with both bulk components and filler could be useful for the joining process. For both joints W–W and W–EUROFER, demonstrators were successfully fabricated and analyzed by metallurgical and physical methods (see Fig. 5).

Solid state diffusion bonding is considered for joining tungsten to ferritic/martensitic steel (EUROFER97) parts. Investigations were performed on the applicability of this technique using low activation vanadium interlayers. Since EUROFER97 contains some amounts of carbon, the problem is to prevent the formation of brittle vanadium-carbide layers. It was demonstrated that diffusion
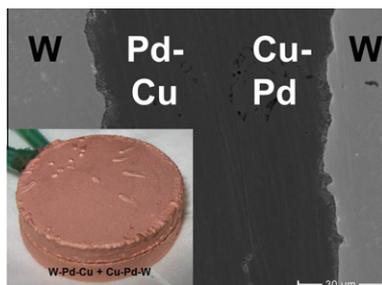
Fig. 6. Cross-section of a composite formed by laser spraying of tungsten powder on bulk stainless steel substrate. Backscattered electron image (tungsten = bright phase, steel = dark phase).

Fig. 7. Cross-section of an FGM formed by hot pressing of tungsten and stainless steel powders. Backscattered electron image (tungsten = bright phase, steel = dark phase).

bonding at only 700 °C can be successfully performed with a minimal alteration of the microstructure of the base materials and strongly reduced formation of vanadium-carbide. These yield to joints with high strength, ductility and toughness.

Graded transition joints from steel to tungsten might be useful for attaching the armour (tungsten) to the first wall (EUROFER 97). Finite element simulations showed that functionally graded interlayers could also be beneficial for joining tungsten and steel parts, such as the thimble in the He-cooled divertor [12,13]. Magnetron sputtering, vacuum plasma as well as laser spraying, and hot pressing processes were applied for this purpose. The first two mentioned production methods are capable of depositing tungsten/EUROFER97 coatings at a porosity level lower than 4% on WL10 substrates. Thus the mixing ratio covers a range from 33 at.% W to 87 at.% W for magnetron sputtering and the full range for VPS.

Laser spraying with tungsten powder succeeded in producing dense tungsten–steel composites with uniform distribution of the phases (Fig. 6). Depending on the composition and laser scanning pattern, thermal conductivity ranged from 22 to 40 W/m K; this was further improved by annealing or laser post-treatment up to

Fig. 5. Microcut of tungsten which was first electrochemically coated with a Pd layer and then with copper. After brazing two pieces together, the material sequence is W–Pd–Cu/Cu–Pd–W. The inserted image shows the Pd/Cu-coated tungsten discs before joining.
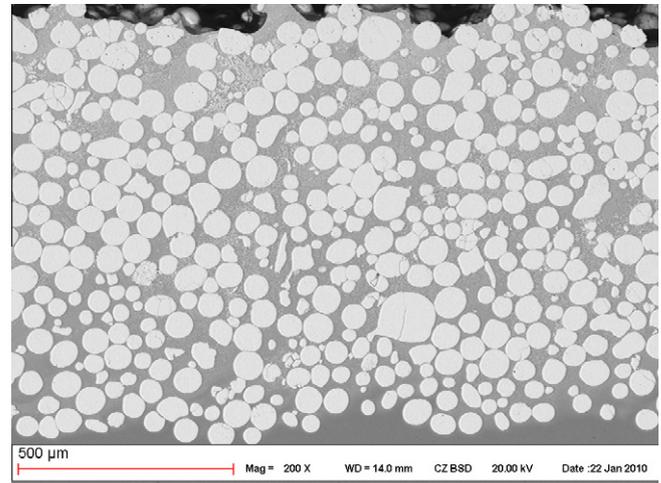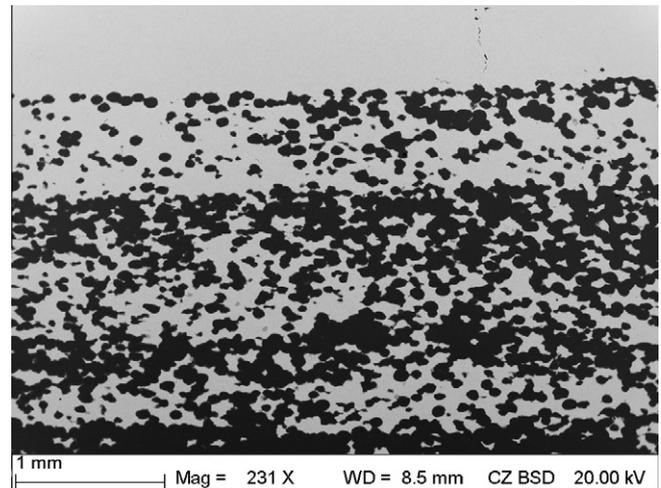
about 50 W/m K. Graded layers with a fully tungsten surface were formed, but the top tungsten layer retained some porosity. Among the advantages of this technique are a limited heat input to the coated part and the ability to coat complex shapes. The hot pressing of tungsten and steel powder mixtures was used as an alternative approach. Fully dense homogeneous composites and graded layers were produced (Fig. 7). The thermal conductivities were, as expected, close to bulk materials, ranging from 25 (100% steel) to 168 W/m K (100% W). In both types of composites (laser sprayed and hot-pressed), formation of intermetallic phases were observed at the tungsten/steel interfaces. XRD measurement showed the presence of Fe_7W_6, Fe_2W_2C and Fe_3W_3C [14].

Plasma spraying offers the advantage of easy control of the compositional profile and the ability to cover much larger areas than the other techniques [15]. Relatively low thermal conductivity, due to the lamellar microstructure and porosity, remains the main limitation of this technique. While spraying in air, in-flight oxidation of the molten metallic powders is probably the main cause of this [16]. Vacuum plasma spraying can be used [17], but with significant increase in equipment and operational costs. In the current investigation, plasma spraying with a hybrid water–argon plasma torch, including inert gas shrouding, was explored [18]. Pure steel and tungsten coatings were produced in a variety of conditions and characterized. The best conditions were selected for the production of composites and functionally graded materials (FGMs), whose characterization is under way. Various kinds of post-treatment are being considered, with the aim of improving conductivity. So far drawbacks have been identified in the limitation of the process temperature due to porosity, grain coarsening, and formation of intermetallic phases and the restricted scalability of the whole fabrication to large-scale components.

For brazing tungsten, pure titanium, Ti–Fe and ternary Ti–Cr–Fe filler materials were used to fabricate the joints. Two techniques were used for manufacturing the fillers. (1) Ti and Fe were melted in a vacuum furnace and brazing foils produced of the castalloy. (2) Thermal spraying by high velocity oxy-fuel (HVOF) was applied to produce different brazing layers (Ti–Fe, Ti–Cr–Fe) on the tungsten base metal. In the first case, pure metallic powders were mechanically mixed, compacted, and melted to allow for brazing filler materials with homogeneous compositions.

Fillers with the same composition but fabricated by HVOF thermal spraying had lamellar microstructure, although it was observed that parts of the Fe powders suffered from surface oxidation which prevented the complete melting of the filler during the brazing process. One way to reduce this effect was to increase the ratio of H_2/O_2 in the HVOF flame producing the Ti–Fe layers, which means using a more reducing atmosphere.

The best brazed joints were obtained using fillers fabricated by the melting route (1). W substrates which were joined with thin brazing foils of 200 μm thickness Ti–86Fe produced a continuous

interface (see Fig. 8a). Nevertheless, various brazing defects could be detected in the W–W joints by closer microstructural examination: (1) pore formation within the solidified braze, (2) dissolution of W base material in the filler, (3) partial dissolution of the W grain boundaries and (4) formation of brittle intermetallics. This can be clearly recognised in the magnified micrograph of a Ti–46Fe braze in Fig. 8b. Preliminary results of mechanical characterization of these W–W joints using Ti–Fe fillers gave rise to an average shear strength of 140 ± 8 MPa. These values are better than those obtained by other studies using sheets of commercial titanium (102 ± 11 MPa) [19], although W–W joints using Ti–Fe fillers showed higher porosity.

Yet another alternative to brazing is the use of pulse plasma sintering/welding. This method was applied to join tungsten tiles directly to WL10 thimbles. The first microstructural examinations have shown areas of perfect joints but also some gaps. Pulse plasma sintering was also used for joining a WL10 thimble to a EUROFER pipe. For the circumferential joint a 100 μm iron foil was put between the thimble/pipe and the conical sleeve. Also here, the microstructural examinations have shown some gaps. Nevertheless, this seems to be a promising process worthy of further refinement by on-going investigations and developments [20].

3. Structural tungsten materials

The main requirements of tungsten materials for structural divertor applications comprise properties like high thermal conductivity, high temperature strength and stability, high recrystallization temperature, and enough ductility for an operation period of about two years under enormous neutron load. The investigations made during recent years have shown that creep strength and recrystallization can be improved with only little effect on thermal conductivity by the use of dispersed oxides such as lanthana or yttria which stabilize the grains. The intrinsic brittleness of tungsten (measured by Charpy tests), however, cannot be improved by oxide dispersion. On the contrary, inter-crystalline fracture is enhanced even more.

Furthermore, it was shown that, due to its distinct anisotropic microstructure, tungsten rod material is useless for most structural applications, such as pipe fabrication. Plates also show anisotropic behaviour. Nevertheless, with thin plates the microstructure can very easily be aligned to the contour of the according part (e.g., by bending or deep drawing, see Fig. 2) which leads to the optimum stress distribution and, therefore, to the best possible fracture behaviour [21].

However, the brittleness (measured by Charpy or by fracture mechanics tests) of tungsten materials is still the main problem for their use as structural materials. And due to neutron irradiation the shift of ductile-to-brittle transition temperature (DBTT) can
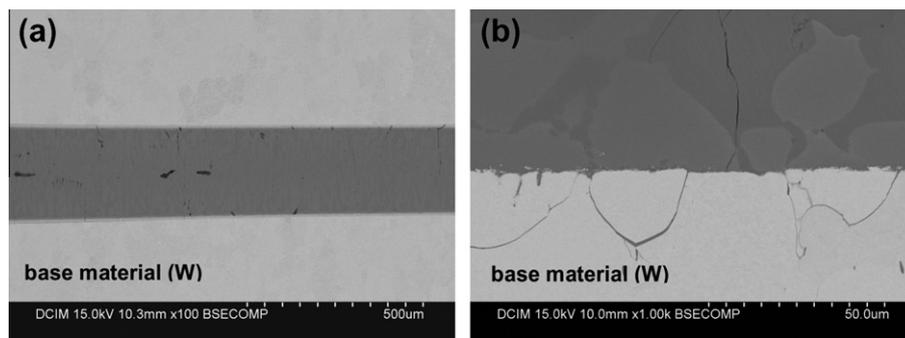

Fig. 8. SEM images of W–W joints using (a) Ti–86Fe and (b) Ti–46Fe brazing foils. Both joints were produced in a vacuum furnace at temperatures slightly above the melting temperature of the brazing materials.

certainly be in the range of several hundred degrees. Therefore, the most pressing question is: How can DBTT be significantly decreased?

3.1. Ductilisation

In principle, there are three ductilisation strategies that were followed in the present programme, which are (1) alloying/solid solution, (2) nanostructuring, and (3) producing composite materials.

So far, only rhenium is known to improve the ductility of tungsten by solid solution but its use for fusion energy applications has been ruled out for reasons of cost and irradiation embrittlement. Iridium too is sometimes mentioned in literature as having a similar effect [22], though it is even more expensive. This leaves only tantalum, vanadium, molybdenum, and titanium which also form solid solution with tungsten (Cr is excluded from this list since W–Cr alloys are known for their brittleness). Round blanks of W–1%Ta, W–5%Ta, W–5%V, W–25%Mo, and W–50%Mo have been produced by PLANSEE (sintered in hydrogen atmosphere and forged to a deformation degree of 80%). Charpy tests in the temperature range of 400–1100 °C (in vacuum) have shown that compared to pure tungsten the DBTT of all alloys is higher, i.e. they are more brittle. Therefore, it is assumed that tungsten cannot be ductilised by solid solution, except with rhenium (or maybe iridium). As a

last option, however, the effect of titanium has still to be investigated.

To back up this conclusion, four-point fracture tests have been carried out on the W–5%Ta material and on an ultra-high purity tungsten grade (UHP-W). Both alloys were produced by PLANSEE SE. After sintering in hydrogen atmosphere, the bars were forged to round blanks with a diameter of 180 mm and thickness of 30 mm. The deformation degree was about 80% in both cases and the purity of the UHP-W batch is higher than 99.999%. The study was carried out to demonstrate the adverse influence of tantalum alloying additions on the fracture properties of tungsten alloys by a fracture mechanics test with a much lower strain rate compared to the above-mentioned Charpy tests. Samples in both the longitudinal-short transverse (LS) and short transverse-transverse (ST) orientations of size 1 mm × 1 mm × 12 mm, as used in several previous studies on pure tungsten [23–25], were manufactured by spark machining followed by polishing to a 1 μm diamond finish. A notch with sharp cracks at the base was introduced into one surface using spark machining. Samples were tested at a strain rate of $\approx 3.33 \times 10^{-5}$/s at temperatures from 21 °C to 1000 °C. In the ST orientation, with the long axis of the grain structure normal to the principal tensile stress, at room temperature both UHP-W and W5Ta failed in a brittle manner (Fig. 9A). Examination of the fracture surfaces shows an intergranular fracture mode in both materials, with the crack propagating from the notch straight
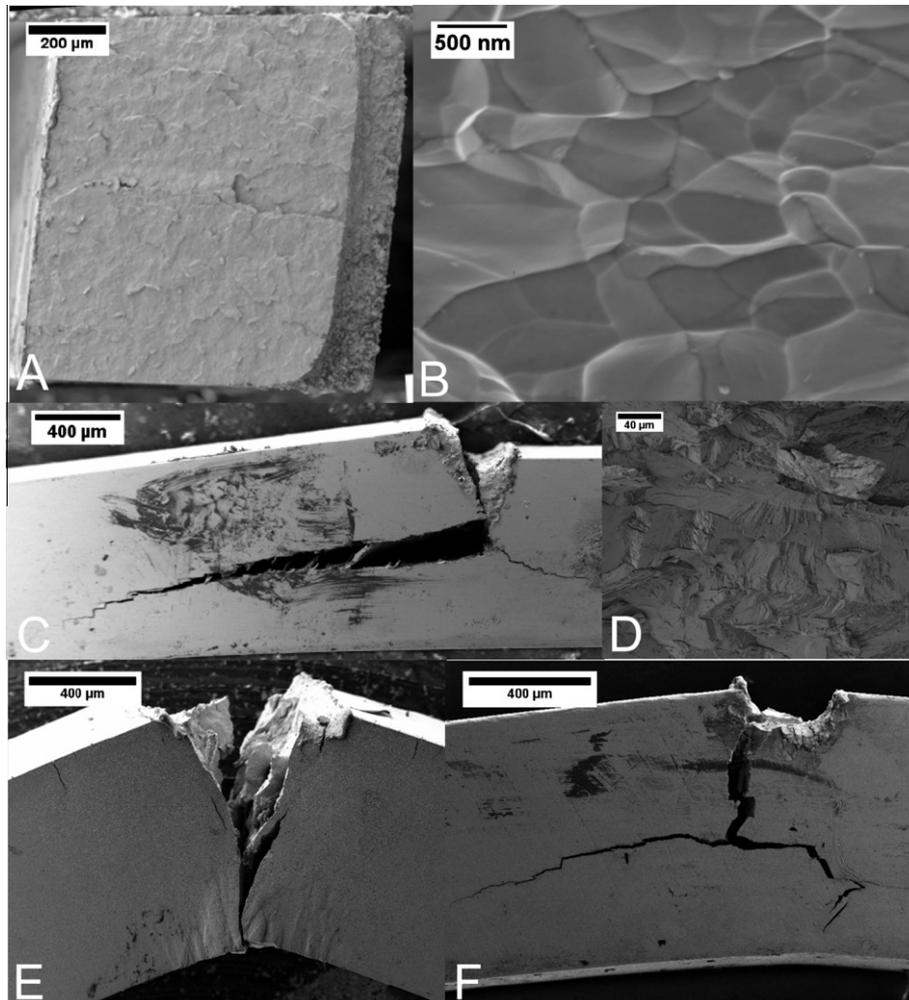

Fig. 9. Fracture surfaces from UHP-W and W5Ta macro-scale fracture surfaces. (A) Room temperature in ST orientation in W5Ta. (B) 900 °C in ST orientation in W5Ta showing intergranular fracture. (C) 900 °C in LS orientation showing delamination of sample. (D) RT in ST orientation in UHPW showing transgranular cleavage. (E) UHP-W in ST orientation at 900 °C showing plasticity in compressive region of sample. (F) UHP-W in LS orientation at 350 °C showing delamination.

Fig. 10. EBSD inverse pole figure map, around delamination crack in W5Ta tested at 600 °C. The crack is seen to follow high angle grain boundaries.
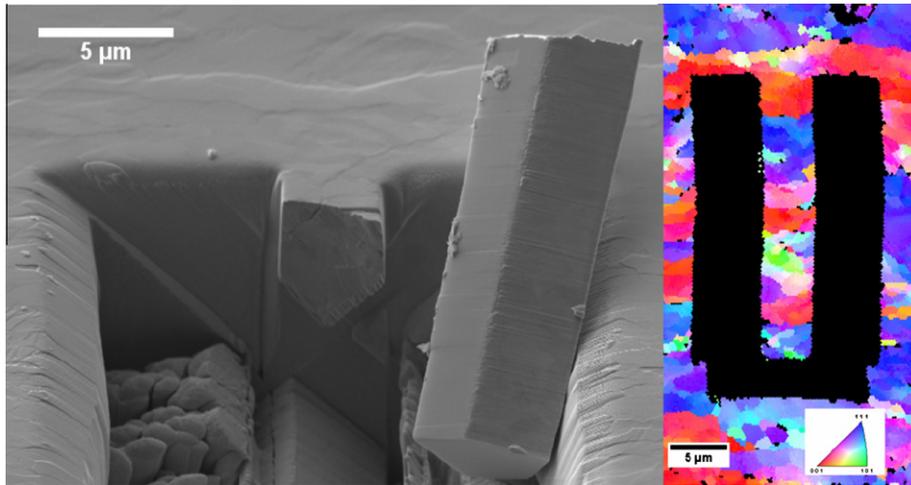

Fig. 11. Tested micro-cantilever manufactured using focused ion beam machining and EBSD IPF map showing position of grain boundary close to fixed end.

through the sample. At 900 °C the W5Ta materials still failed in a brittle intergranular manner (Fig. 9B). However, the UHP-W materials underwent significant plastic deformation in the compressive region of the beam before failure (Fig. 9E), though close examination of the fracture surface shows that the surface is still dominated by intergranular fracture. Fracture in the LS orientation, where the long axis of the grain structure is parallel to the principal tensile stress, is more complicated. At room temperature the W5Ta material failed in a brittle manner. At higher temperatures in the

W5Ta material the samples failed by a 'delaminating' mechanism (Fig. 9C). The crack starts from the notch base, but then propagates along the length of the sample normal to the direction of bending; however, examination of the surface again shows it is dominated by grain boundary fracture. The UHP-W in the LS orientation shows a transgranular cleavage fracture surface at room temperature (Fig. 9D). At 450 °C this has changed to a 'delaminating' type mechanism, as seen in the W5Ta material, although plastic deformation is also seen in the compressive region below the notch
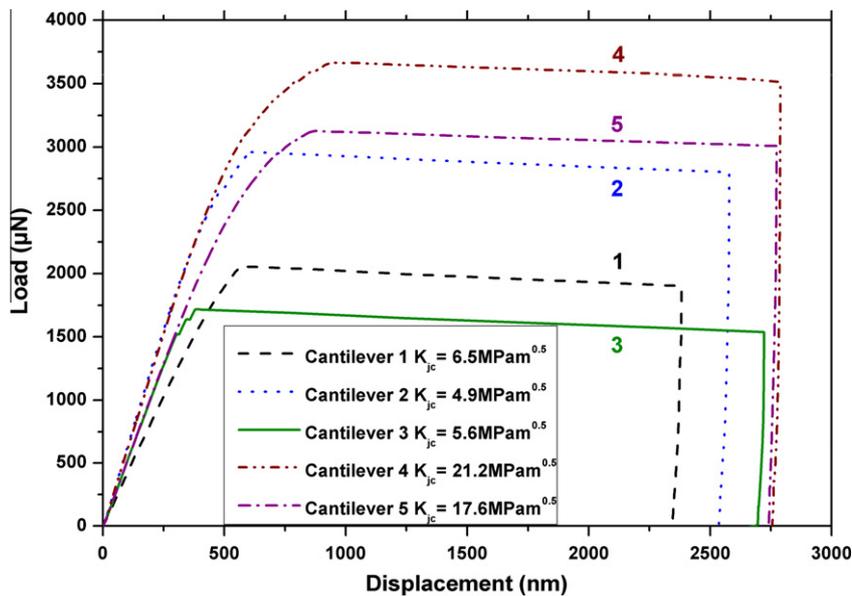

Fig. 12. Load displacement curves for tested W5Ta micro-cantilevers.

(Fig. 9F). EBSD around the crack path of one delaminated sample of W5Ta (Fig. 10) shows that fracture is dominated by failure between the high angle grain boundaries, with no fracture at low angle boundaries. Micro-mechanical fracture testing of selected grain boundaries is currently being used to understand which grain boundaries control the strength of the samples. Focused ion beam machining has been used to manufacture small cantilevers ($\approx 25\,\mu m \times 4\,\mu m \times 6\,\mu m$) (Fig. 11), which are then deflected to fracture using a nano-indenter, to measure the fracture toughness of single grain boundaries [26–28]. Initial results (Fig. 12) show a range of fracture toughness values from 5.6 to 21.2 MPa m$^{0.5}$. Further investigations into the effect of grain boundary crystallography and chemistry are currently on-going, but it appears that tantalum has no beneficial effects, and may even have detrimental effects, on the fracture properties of tungsten.

Nanostructuring of tungsten and tungsten alloys has been investigated in the past by severe plastic deformation (e.g., by high pressure torsion, HPT). But these processes are not suitable for producing industrial-scale semi-finished products. That is why in the present programme powder metallurgical fabrication routes were followed, which include mechanical alloying and hot isostatic pressing and/or hot/cold forming.

The investigated materials comprise pure W, W–Ti, W–V and W–Ta alloys. In some cases they are reinforced with Y_2O_3, La_2O_3, or TiC particles (see, for example, [29]). It was found that all the materials are composed of small grains, with sizes ranging between 20 and 500 nm, and show a high density (5.4–$6.9 \times 10^{22}\,m^{-3}$) of small Y_2O_3 or TiC particles, with sizes between 1 and 50 nm. In the case of W–Y materials, all the Y transformed into Y_2O_3 during mechanical alloying, due to the high amount of O (around 1 wt.%) present in the milled powders, which is beneficial for reducing the excess O content in the materials. All the materials also contain a residual porosity of a few per cent, which is typical of materials compacted by a HIP cycle, and they exhibit high strength and a promising radiation resistance. However, in spite of their small grain sizes, they are very brittle and show poor fracture properties at low to moderate temperatures. For instance, the DBTT of the W–Y, W–Ti and W–V materials was found to lie typically in between 1100 °C and 1200 °C, which can be considered as additional proof of the previously mentioned effect of solid solution elements. Due to the fabrication route, missing mechanical working and/or an increased impurity level could also be an additional explanation for this severe brittleness.

W–2%Y_2O_3 material was produced by sintering and hot forging in collaboration with PLANSEE [30]. The relative density of the ingot was found to equal 99.3%. The material appears composed of grains with a mean size around 1 µm and also contains Y_2O_3 particles with sizes ranging between 300 and 900 nm. Fracture mechanical three-point bending and tensile tests showed that the material is fully ductile in the temperature range of 300–1000 °C, the total elongation ranging between about 4% and 10%.

An alternative route to fabricate nanostructured tungsten-based materials is by chemical powder metallurgical methods. A precursor powder containing the required elemental composition can be prepared in aqueous solution from atomic or molecular level under controlled conditions to engineer particle characteristics such as size, composition and structure. The obtained precursor is thereafter further reduced under hydrogen and sintered into the final tungsten composite. Several tungsten materials containing 1% of La_2O_3 or Y_2O_3 have been produced using an early development of the method [31] in which La- or Y-ions mainly occurred on the surface of the precursor particle, resulting in an inhomogeneous distribution of the doping elements in the sintered material. In a recent development, precursor powders are fabricated under certain solution conditions where the particle growth could be
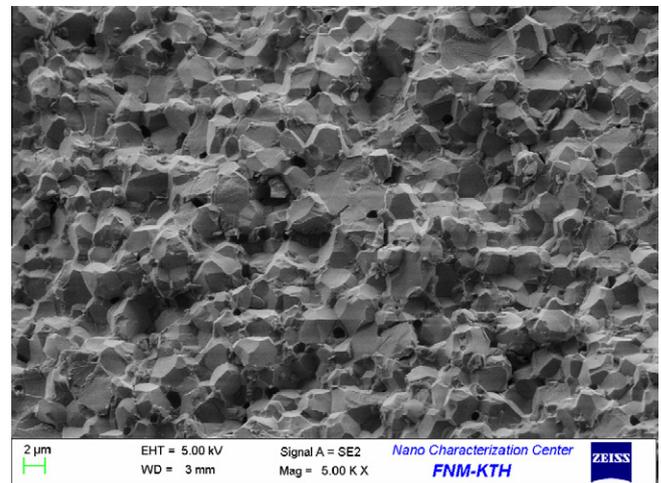

Fig. 13. Fractured surface of sintered W–1%Y_2O_3 with uniform grain size of about 3 µm.
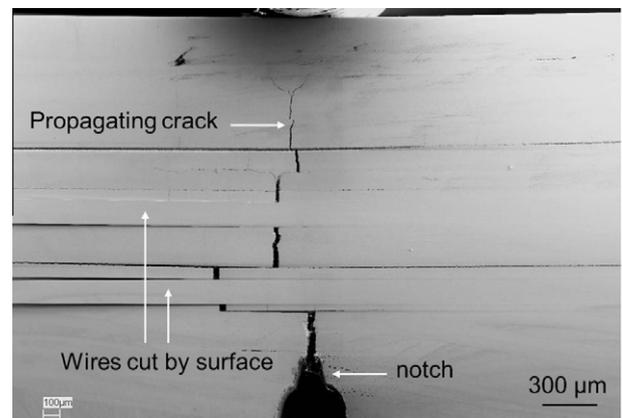

Fig. 14. Cross section of a many-fibre W/W composite specimen after 3-point bending test. Crack propagated in a stable manner as the reinforced wires bridged the crack face.

controlled to produce uniformly yttrium doped nano-sized tungsten oxides. The starting material, ammonium paratungstate with a particle size of 30–100 µm, is transformed under acid solution conditions via a solvent-mediated process into precursor powders with a crystallite size of less than 10 nm. These powders have been reduced under hydrogen to nanostructured tungsten-ODS powders (1–5% Y_2O_3) and sintered to ultrafine- or fine-grained tungsten composites with up to 95% relative density, uniform with respect both to microstructure and composition (see Fig. 13). The method can produce extremely uniform materials, with respect to morphology as well as composition. On-going work considers further optimization of powder processing and consolidation in order to limit grain growth from the precursor to the final material.

To enhance fracture toughness of tungsten, tungsten-fibre reinforced tungsten composites (W_f/W_m-composite) were developed [32–34]. A novel method of chemical vapour infiltration (CVI) of tungsten was developed to fabricate these composites [35]. The applied toughening mechanism is analogous to those being used in fibre reinforced ceramic matrix composites (FCMCs), so-called pseudo toughness. A controlled crack deflection at the engineered fibre/matrix interfaces leads to internal energy dissipation by interface debonding and friction. Local stress can be reduced and thus the global fracture toughness is improved [36]. The interface debonding was directly

observed by high energy synchrotron tomography during mechanical tension tests [37]. Recently the pseudo toughness behaviour was shown in a three point bending test (according to ASTM E399) as shown in Fig. 14. The specimen contained about 90 unidirectionally orientated fibres resulting in a fibre volume fraction of about 25% of the bulk matrix material. Pure CVD tungsten (tested in the same way) fails catastrophically after crack initiation while the W_f/W_m composite shows stable crack propagation and a rising R-curve. The fracture toughness K_Q in that area is comparable to pure CVD tungsten at crack initiation, but after that the fracture toughness increases significantly higher than pure CVD tungsten. As determining the crack length is difficult in a composite, the initial, artificial, crack length was taken for calculating K_Q. At a certain point during the experiment a severe event, such as multiple fibre fracture, leads to a large load drop, but not to a full fracture. The sample can still bear load. By further loading, toughening effects like fibre pull-out, internal friction or minor fractures occur. They lead to a large energy dissipation and thus a large improvement in fracture toughness.

In a second concept, the brittle W matrix is reinforced by short fibres of tantalum (initially 100 μm diameter wire). As Ta is more ductile than W it can therefore divert or stop cracks propagating in the W matrix. Elastic and plastic deformations of the reinforcing fibres absorb the elastic energy released by the propagating crack. The major difficulty with this concept is the inter-diffusion between W matrix and fibre during sintering (at temperatures of 1500–1600 °C). One approach is to use spark plasma sintering to reduce the duration of exposure to high temperature to less than 5 min and still achieving 90% densification in a single operation. Service temperature below recrystallization temperature (∼1100 °C) induces negligible inter-diffusion in the composite – especially in the case of Ta fibres [38] (see Fig. 15).

A third approach considers tungsten laminate material which is fabricated from tungsten foils brazed by copper. The composite strategy seems to be rather promising with respect to improving fracture toughness.

3.2. Characterization for W data base

For clear comparability all the produced materials have to be characterized by basic, standardized methods which are (1) DBTT
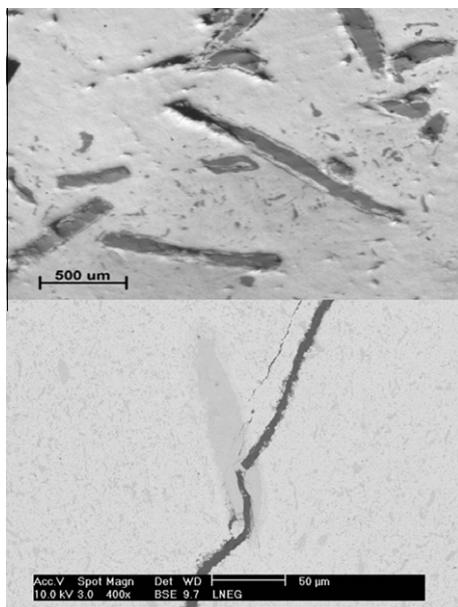

Fig. 15. Upper image: Ta fibres embedded in the W matrix. Lower image: Deflection of a crack by a Ta fibre.
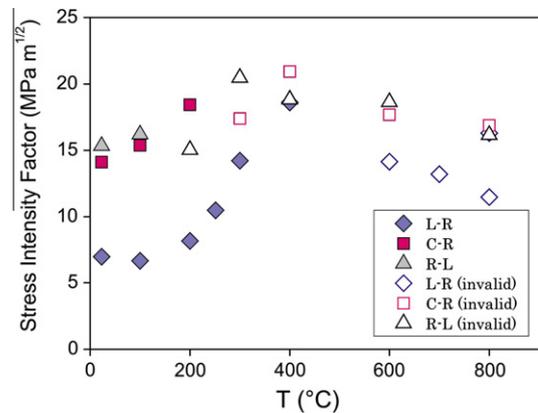

Fig. 16. Fracture toughness of polycrystalline tungsten vs. test temperature for three different specimen orientations [39]. The values denoted by open symbols do not satisfy the ASTM 399 validity criteria due to onset of ductile behaviour. (They mark only a lower bound of fracture toughness K_{Ic}.)

measurement either by Charpy or by fracture mechanics tests, (2) creep/tensile/indentation tests up to 1300 °C, (3) thermal conductivity measurements, (4) determination of re-crystallization temperature, and (5) microstructure and fracture analysis. Within the present EFDA programme, commercial grade tungsten materials are used to establish a database for future recording of the progress in material development. Here is an example for the fracture toughness (FT) measurement of a round blank of pure tungsten where the specimens were oriented longitudinally (L-R), radially (R-L) and circumferentially (C-R) [39]. The fracture mechanical experiments yielded distinctive fracture behaviour for each investigated specimen orientation. For the longitudinal orientation the material exhibited a low room temperature FT of about 7 MPa m$^{1/2}$ and a steep increase of fracture toughness above 200 °C (see Fig. 16). For the radial and circumferential orientations, in contrast, the material exhibited relatively high room temperature FT of about 15 MPa m$^{1/2}$. Fracture mechanical behaviour of round blank polycrystalline tungsten with good fracture toughness values in two of three investigated orientations is superior to fracture mechanical behaviour of commercially available polycrystalline tungsten rods with only one strong orientation [40]. Indeed, in the latter case only the specimens extracted in L-R orientation showed a room temperature fracture toughness of about 15 MPa m$^{1/2}$.

4. Tungsten armour materials

The range of operating temperature and load conditions (pulse, fatigue, shock, flux, etc.) depend strongly on the power plant design and cannot be exactly specified yet. However, the lowest armour temperatures can be expected to be somewhat higher than the maximum coolant temperature, i.e. about 800–900 °C in the case of the helium-cooled finger design and about 500 °C for the blanket's first wall. The maximum temperatures will certainly be higher than 1700 °C on the divertor armour surface.

With that, the most important questions in this line of research are: How can the sputtering rates and surface modification mechanisms of tungsten armour materials be simulated by existing test facilities? Are there optimal tungsten materials for armour applications? Is there a possibility to utilize oxidation-resistant tungsten alloys to increase safety in the event of air ingress in accident scenarios?

4.1. Heat flux, shock and high temperature testing

Besides basic material characterization in an extended high temperature range (including thermal fatigue), thermal shock tests
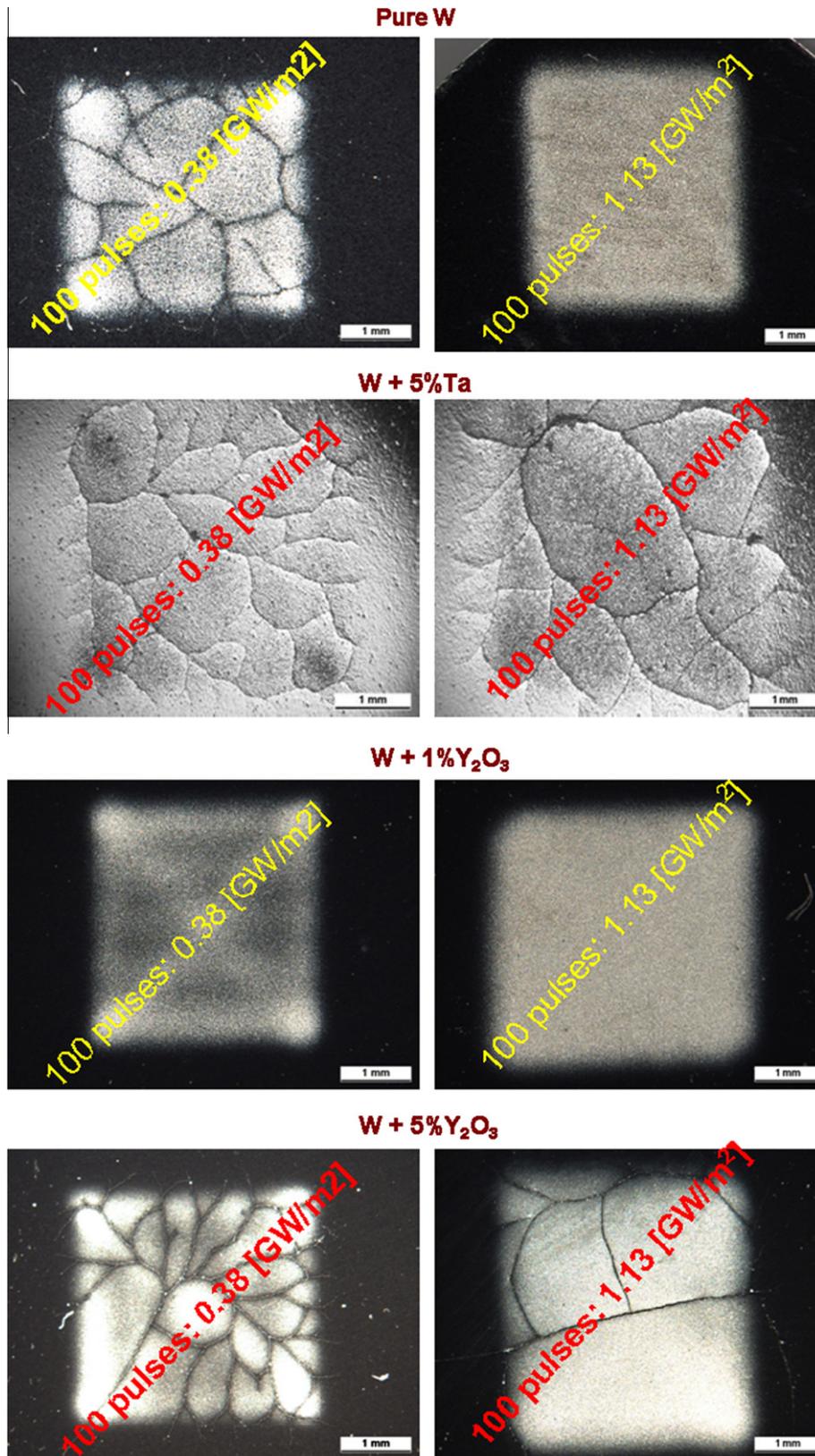
Fig. 17. Surface of different metal injection-moulded W alloys after high heat flux testing at RT with 100 pulses and power densities of 0.38 and 1.13 GW/m². W–1 vol.%Y$_2$O$_3$ performed best in the tests so far. (The surface of pure tungsten shows also a network of fine cracks after loading with 1.13 GW/m², but this can only be recognized at higher resolutions.)

in the operation relevant parameter range (JUDITH electron beam facility, FZ Jülich [41]) and thermal fatigue tests under hydrogen and/or helium neutral beam loading (GLADIS, IPP, Garching [42,43]) with divertor relevant power fluxes were carried out.

The thermal shock effect of possible edge localized modes (ELMs) in the plasma on various new metal injection moulded (PIM) armour materials was simulated in the JUDITH facility. The incident power flux was varied between 0.19 and 1.13 GW/m^2, the test temperatures were room temperature, 200 °C, and 400 °C, and the specimens were loaded with 100 (in some case even 1000) pulses with a duration of 1 millisecond. The most promising material so far is W–1 vol.%Y$_2$O$_3$ showing as yet no crack formation, while pronounced cracking is observed in W–5 vol.%Y$_2$O$_3$ and W–5 wt.%Ta materials under similar loadings (see Fig. 17). Moreover, the JUDITH 2 facility was used for investigations on high cycle thermal shock tests (up to 10^6 cycles) with the tungsten reference material. First results revealed that surface roughening inevitably leads to crack development and subsequently to melting at crack edges.

A comparative study of surface morphology changes of W materials under cyclic hydrogen and helium beam loading was performed with the GLADIS facility at IPP Garching. In the frame of the European material development programme for DEMO, W containing 5 wt.% Ta as well as uniaxially forged UHP-W, and PIM tungsten were assessed. Complementary to the thermo-mechanical investigation of the high heat flux behaviour of W as a plasma facing material, the investigation of the morphology modification, is important in order to develop reliable armour materials. This occurs during heat loading using H and He particles, which simulates the expected steady-state DEMO divertor operation conditions. Effects of erosion, gas retention, and void formation depend on both the loading conditions and the operating temperature. Actively cooled W samples were loaded under two conditions: (1) with pure H and (2) with a mix of 90 at.% H and 10 at.% He (flux 2 × 10^{21}/m^2 s). The applied 10 MW/m^2 thermal load resulted in surface temperatures between 1500 °C and 2000 °C depending on the sample design. Particle fluences up to 3 × 10^{25} atoms/m^2 under stationary temperature conditions were reached by repeated pulses of 30 s each. All tested materials were completely recrystallized after less than 1 h loading. For both surface temperatures, 1500 °C and 2000 °C, a substantial grain growth was observed (see Fig. 18). The initial anisotropic grain orientation of the materials has disappeared in the samples heated up to 2000 °C. Only grain growing and physical sputtering were identified as the surface modification processes of the pure hydrogen loaded materials (Fig. 18). Thermally induced cracks in the bulk material did not occur. In case of the mixed H/He loading, the 10% He fraction dominates the surface morphology changes. A high number of voids were identified up to a depth of about 1 μm below the surface (see Fig. 19). Due to the porous surface structure the effective armour surface is reduced (compared to a plane surface). Therefore,
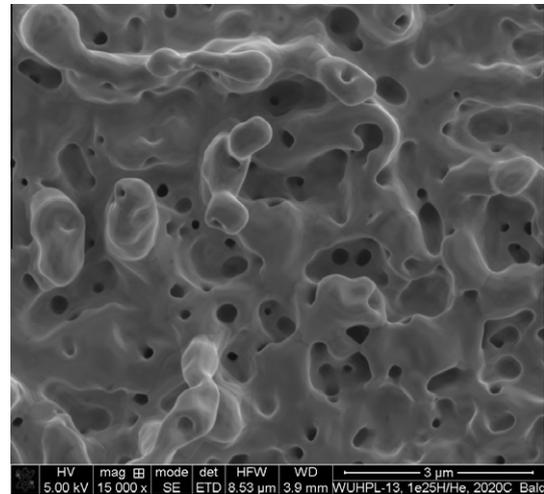

Fig. 19. Surface modification (significant erosion and high void density) of the same material as in Fig. 18 (UHP-W round blanks) after DEMO diverter relevant 90% hydrogen/10% helium loading (10 MW/m^2, 10^{25} atoms/m^2) for 2500 s at 2020 °C.

an enhanced erosion rate of the plasma facing material had to be taken into consideration for the operating conditions of a DEMO power plant. After validation by further tests, this would be a very important result with a high impact on the power plant design.

4.2. First wall armour materials

The use of tungsten as first wall (FW) armour of a fusion power reactor represents an important safety concern in the event of an accidental loss of coolant together with simultaneous air ingress into the reactor vessel. During this scenario, temperatures up to 1200 °C could be achieved in the in-vessel components due to the decay heat [43], which would lead to fast tungsten oxidation with the release of volatile radioactively activated tungsten oxides. The linear oxidation rate of tungsten at 1000 °C is about 1.4 × 10^{-2} mg cm^{-2} s^{-1} [44], which in the approximately 1000 m^2 DEMO first wall would correspond to a release of half a ton of tungsten oxides per hour. A way of avoiding this problem is the addition to tungsten of oxide-forming alloying elements leading to the growth of a self-passivating layer at high temperature in the presence of oxygen. During normal operation, the surface of this material will consist of pure tungsten, owing to preferential sputtering of the alloying elements. In previous studies
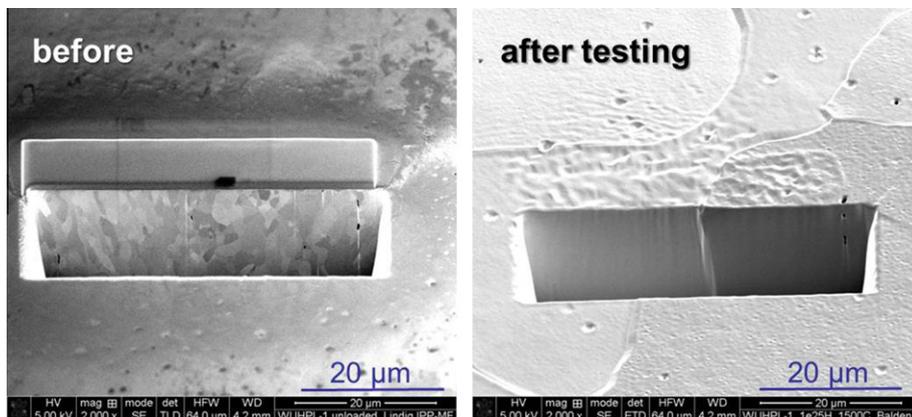

Fig. 18. Surface structure and cross-section of ultra-high purity tungsten (UHP-W) round blanks before and after hydrogen loading (10 MW/m^2, 10^{25} atoms/m^2) for 2500 s at 1500 °C.

Table 1
Composition and results of the screening oxidation tests with different tungsten-based alloys at 1073 K for 3 h.

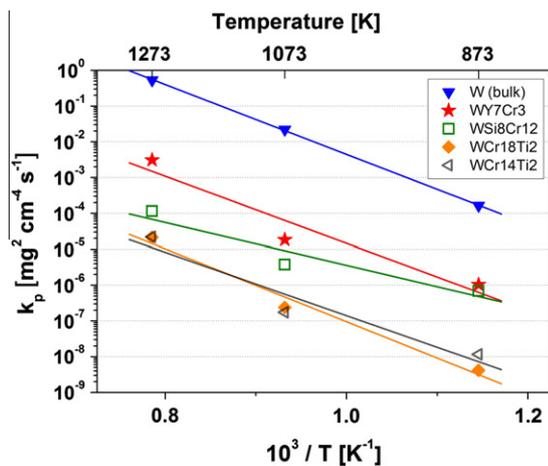| Alloy (wt.%)	Oxidation test result
W–Cr14–Ti2	Slow oxidation
W–Cr18–Ti2	Slow oxidation
W–Cr16–Zr9	Film delamination
W–Hf17–Ta15	Film delamination
W–Hf32–Ti2	Film delamination
W–Ta12–Ti2	Film delamination
W–Ta12–Zr5	Fast oxidation
W–Zr2–Ti1	Film delamination
W–Y7–Cr3	Relatively slow oxidation
W–Y24–Cr2	Film delamination

Fig. 20. Arrhenius plot of the parabolic oxidation rates (k_p) of pure tungsten and different tungsten-based alloys. The k_p value has been calculated from the quadratic weight increase per area versus time in a linear fit.

the good performance of the system W–Cr–Si manufactured via magnetron sputtering could be demonstrated [45]. Thin films of such alloys showed a strongly reduced oxidation rate compared to pure tungsten. However, the formation of brittle tungsten silicides may be disadvantageous for the powder metallurgical production of bulk W–Cr–Si alloys if a good workability is needed. Screening tests have been carried out (see Table 1 and Fig. 20) to identify suitable silicon-free alloys with distinctive self-passivation and a potentially good workability [46]. Of all the tested systems, W–Cr–Ti alloys showed the most promising results. The oxidation rate was even lower than that of the WCr12Si8 alloys. The weight

loss was about four orders of magnitude lower than with pure tungsten. This performance could be conserved even if the content of alloying Cr was reduced from 18 wt.% to 14 wt.%. Since thicknesses of several mm are required for the FW armour, bulk alloys have been manufactured by powder metallurgy (mechanical alloying +HIP), the composition of which was based on the results obtained by thin films; so far, bulk alloys of compositions WCr10Si10 and WCr12Ti2.5 have been produced, achieving nearly 100% dense materials in both cases [47,48]. The microstructure of the WCr10Si10 material (Fig. 21, left) is very homogeneous, with grain sizes of a few 100 nm, and consists mainly of a $(W,Cr)_5Si_3$ mixed crystal together with some pure W grains and isolated SiO_2 grains. In addition, an ultrafine ODS-like phase inhibiting grain growth is detected. The oxidation rate of this alloy is lower than that of the corresponding thin films at 600 °C, though higher at 1000 °C [49]. The thermal and mechanical properties of this material are dominated by the silicide $(W,Cr)_5Si_3$; it shows a thermal conductivity of about 16 W/m K at 500 °C and a sharp ductile-to brittle transition in the range 1000–1050 °C. The microstructure of the WCr12Ti2.5 bulk alloy is even more homogeneous and consists of a W-rich and a Cr-rich bcc phases with Cr and W in solid solution, respectively, and some ω-Ti (Fig. 21, right). Other than in the WCr10Si10 material, no intergranular ODS phase inhibiting grain growth was detected in this system, and thus the grain size is slightly larger but still below 500 nm. The thermal conductivity of the WCr12Ti2.5 alloy is close to 50 W/m K in the temperature range of operation (500–600 °C). It exhibits significantly higher strength and lower DBTT (around 900 °C) than the WCr10Si10 material [48]. The oxidation behaviour of the WCr12Ti2.5 alloy is similar to that of the WCr10Si10 material; in this case the oxidation rate is similar to that of thin films of same composition at 600 °C but higher at 800 and 1000 °C [49]. The oxidation mechanism, with the formation of Cr_2WO_6 protection scales instead of the Cr_2O_3 scale found with thin films, is not yet clearly understood. In the on-going programme, the focus is on mock-up fabrication using these bulk materials as armour.

Vacuum plasma-sprayed tungsten (VPS-W) is a coating candidate in the design of first wall components which are expected to face a moderately high heat-flux [15]. It combines the advantages of W as first wall material with the ability to coat large areas and the possibility to repair damaged parts. In this context, tomographic bulk data on the full coating system (2 mm pure VPS-W joined with a 500 μm mixed W/steel interlayer to a EUROFER steel substrate, actively cooled during plasma spraying. Details are given in [17]) can greatly help to improve the understanding of the complex mechanisms governing heat transfer, damage and failure of the coating. Synchrotron-radiation computerized microtomography (SRμCT) offers the advantage of non-destructive imaging of relatively large material regions at high spatial resolution and can be used to feed micromechanical models. However, applying SRμCT
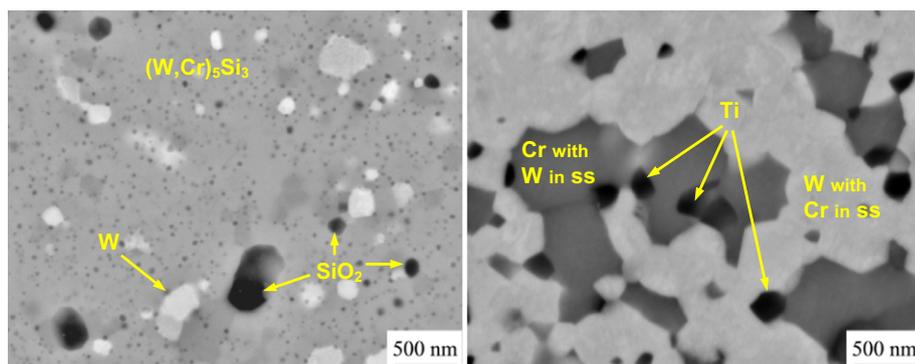

Fig. 21. BSE-SEM images of a WCr10Si10 sample (left) and a WCr12Ti2.5 sample (right) after HIP [47,48].
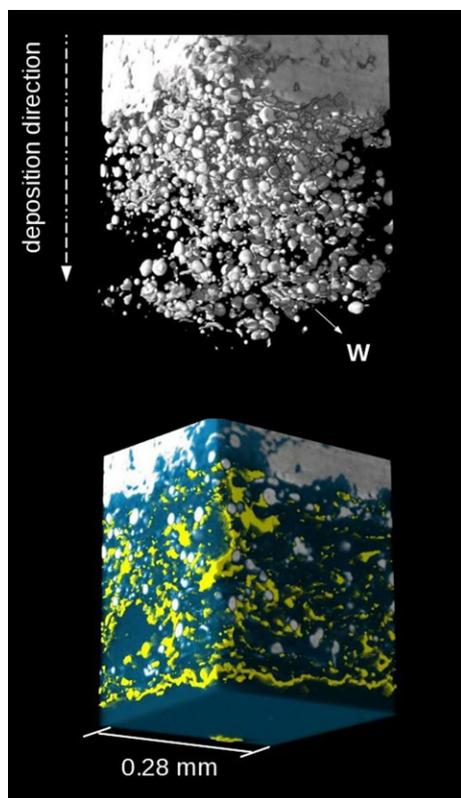
Fig. 22. Three-dimensional renderings of tomography data showing the interlayer region of a VPS-W/EUROFER sample [52]. The volume shown was cropped by software from the original volume data of the full cylindrical sample. Top: the W phase in the interlayer and part of the VPS-W coating. Bottom: combined representation of the EUROFER steel phase (blue), tungsten phase (white), and pore space (yellow). (For interpretation of the references to colour in this figure legend, the reader is referred to the web version of this article.)

to heterogeneous materials with a considerable amount of W is challenging because of the strong X-ray absorption and scattering from W, a dense metal with a high atomic number (Z = 74). Compared to other lower-Z metals, this limits the maximum sample size for investigation by SRμCT and requires the use of high X-ray photon energies, at which it is difficult to maintain sufficient spatial resolution. Experiments conducted at the beamline ID-19 of the European Synchrotron Radiation Facility (ESRF) [50] with 52 keV X-rays and a detector pixel size of 1.4 μm revealed the complex internal phase arrangement of a highly porous (25 vol.%) VPS-W joined to a EUROFER steel substrate (see Fig. 22). Details of the experiment are reported in [51,52]. The coating provided by PLANSEE is made of a top layer (1.8 mm) of porous W and an interlayer region (also plasma-sprayed) where steel and W droplets were co-deposited on the actively cooled substrate [53]. The coating survived 720 cycles under a heat load of 2 MW/m^2 [54]. A tomographic reconstruction of the interlayer region extracted from a cylindrical sample (diameter ∼0.6–1 mm) is shown in the figure. The transition zone from VPS-W to interlayer is clearly visible. In the interlayer, W-particles are surrounded by the steel matrix. A relatively high porosity was observed, in particular at the interface to VPS-W (up to 35 vol.%). Its origin, however, is still unclear, and further investigations are required to understand the evolution of interfacial and bulk porosity during deposition, operation and sample preparation.

5. Materials science and modelling

As already mentioned, at present only Re (and probably Ir) are known to form ductile tungsten alloys. The intrinsic brittleness

of tungsten is primarily due to the high activation energy of screw dislocation glide. Furthermore, radiation damage data – especially under the relevant divertor operation conditions (i.e. in the temperature range 600–900 °C and up to dose levels of 5–10 dpa) – are very rare. Therefore, the main objective for this research effort is to assist and guide the materials development process. One of the significant objectives for modelling is to identify the origin of the extreme brittleness of tungsten and to explore a range of potential ductilisation treatments. Research also involves modelling radiation effects, for example point defects and He/H accumulation, both in the bulk and sub-surface regions of materials, to help interpret results of bulk neutron and ion beam near surface irradiation experiments.

The most striking question that has still not been addressed is: How does tungsten behave under high neutron doses after significant He/H load?

5.1. Plasticity studies

It is well known that the impurity content (e.g., of S, P, O, C) is among the parameters influencing the fracture behaviour of tungsten. However, as one is dealing with different production routes – especially in the case of material produced for scientific purposes – it is not easy to distinguish between effects of grain size, grain shape, impurity content, etc., on mechanical properties. Nevertheless, assuming a strong decrease of fracture toughness for impure materials induced by low solubility of interstitial atoms and grain boundary segregation, vast regions of intercrystalline fracture can be expected. In a recent study, the fracture surfaces of ten different tungsten materials, differing in processing route and thus in grain size, grain aspect ratio and grain boundary impurity concentrations, were investigated using Auger electron spectroscopy and scanning electron microscopy [55]. The manufacturing conditions are: sintered, hipped, rolled, recrystallized, deformed by high pressure torsion (HPT) and a high purity single crystal, which was HPT-deformed and annealed at different temperatures, resulting in different grain sizes. As expected, the impurity concentration decreases with decreasing grain size. All samples were fractured at room temperature, i.e., in the brittle regime of tungsten. Combining all data on the ratio of inter- vs. transcrystalline fracture, grain shape and grain size leads to inconsistencies when postulating a pronounced grain boundary weakening for high impurity contents. The fracture behaviour is much more dependent on the microstructure – on the grain aspect ratio, grain size, its distribution, and dislocation density. What has to be emphasized is that the observation of large amounts of intercrystalline fracture does not automatically denote deduce impurity-induced embrittlement.

It is known that tungsten features an anisotropic fracture behaviour in the case of the presence of elongated grains, e.g., after rolling, forging and deformation by HPT [56,57]. Additionally, the fracture resistance may increase with crack propagation, which implies that it is not always possible to characterize the material's toughness with one single value such as plane strain fracture toughness K_{IC} or critical energy release rate G_{IC}. Instead, the whole crack resistance curve (R-curve) – describing the dependency of fracture resistance vs. crack propagation – has to be given. The initial part of the R-curve is governed by processes in the immediate vicinity of the crack tip, e.g., formation of selected cleavage planes, fracture of selected grain boundaries or tunnelling of the crack to the next grain boundary (see Fig. 23). In a later stage of testing and in the case of predominant intercrystalline failure, the increase of the R-curve depends on crack bridges appearing, which connect the crack flanks and fail by plastic deformation, thus consuming more energy and leading to an extrinsic toughening. Experimental details are given in [58]. There, temperature-dependent fracture experiments using technically pure tungsten featuring
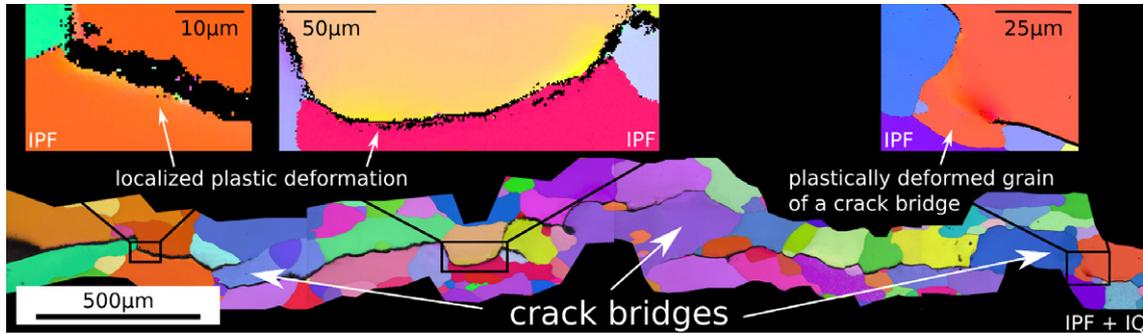
Fig. 23. Electron backscatter diffraction scan of the crack path in a recrystallized specimen in R–L orientation. Coloured inverse pole figure is overlain by an image quality map. The crack grows preferentially at the grain boundaries. A significant change in colour, such as in the right detail, represents localized plastic deformation taking place at crack bridges. The left and centre detail represent transcrystalline and intercrystalline fracture. Taken from [59]. (For interpretation of the references to colour in this figure legend, the reader is referred to the web version of this article.)

recrystallized (globular) and deformed (elongated grains) microstructures are described. R-curve behaviour was found in both cases. Furthermore, the appearance is independent of testing direction, i.e., independent of the dominance of intercrystalline or transcrystalline fracture. However, the increase of the R-curve is rather steep for transcrystalline fracture, when compared to intercrystalline fracture. In addition, pre-deformation of the material and higher test temperatures increase the fracture resistance, i.e., the starting values of the R-curves are higher. For pre-deformation, the initial values of the R-curve are higher; for higher testing temperatures the R-curve behaviour is more pronounced [58,59].

5.2. Simulation

It has been realized that the plastic behaviour and mechanical properties of crystalline materials depend strongly on the properties of dislocations. For bcc crystal structures, low temperature plasticity is governed mainly by the $1/2\langle111\rangle$ screw dislocations due to their low mobility as compared to edge segments. Important features including dislocation-core structure, Peierls stress, slip plane, and dislocation kinks have been obtained for many bcc metals from computer simulations [60,61]. Based on density-functional theory (DFT), the $1/2\langle111\rangle$ screw dislocations in W and its alloys investigated to better understand the basic mechanism of plastic deformation [62]. When the dislocation-core structure in pure W is optimized using both the Quantum-ESPRESSO package and VASP code, a symmetric or non-degenerate core is

revealed. The critical stress, Peierls stress, to move the dislocation in the crystal is calculated and the dislocation is found to slip on $\{110\}$ planes. The results on the dislocation core structure of W–Re alloys with 12, 25 and 50 at.% of Re were compared with those of pure tungsten: Starting from the lowest rhenium content, the dislocations gradually change to an asymmetric or degenerate core structure. The asymmetry becomes more pronounced for higher rhenium contents. Accordingly the Peierls stress is lowered, and the dislocation slips in a zigzag manner on different $\{110\}$ planes which, overall, results in a movement on $\{112\}$ planes (see Fig. 24). These results agree well with the Re ductilizing effect. Other alloying additions in W including Ti, V, and Ta do not induce big changes to the dislocation-core structure. Possible predictions for this transition of core symmetry have undergone further investigation. First, the $\{110\}$ γ-surfaces for W–Ta and W–Re alloys are evaluated, and both exhibit the elliptical distortion. Hence, the core structure is not directly reflected from the γ-surface. Second, the interrow potentials extracted from displacing one row out of a set of [111] atomic rows are examined [63]. It is found that both types of core symmetry can be generated correctly for different alloys using the interrow potential, but the shape of the potential curve remains almost the same when alloying Re in W. Therefore, no criterion for prediction of the core symmetry has been found up to now and the symmetry needs to be determined directly from the geometry optimization.

The ideal tensile strength in the [001] direction of bcc tungsten pure crystal and its alloys (W–Re, W–Ta and W–V) has been
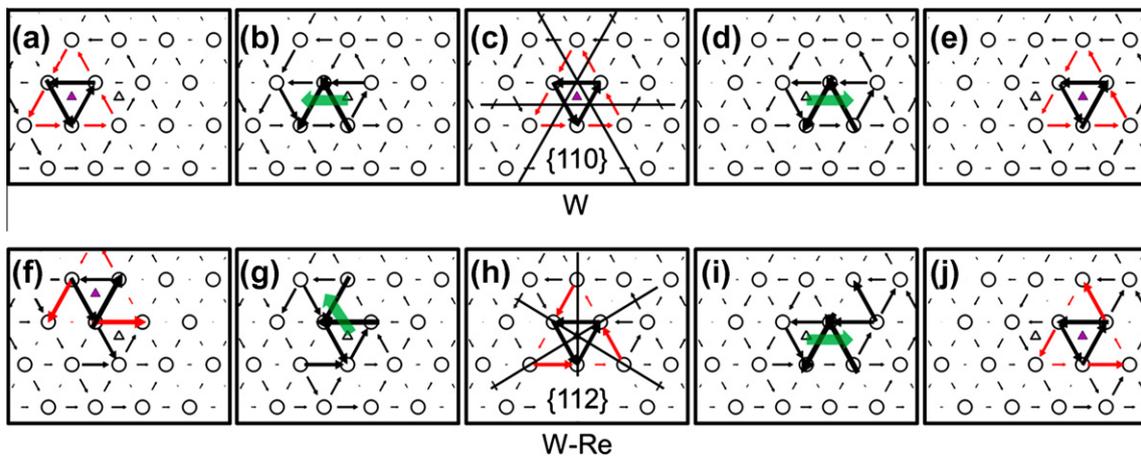

Fig. 24. Snapshots of dislocation-core structures when applying external strain before (middle) and after moving. The pictures left and right of the middle panels correspond to positive and negative strain values, respectively. Empty (filled) triangles mark the initial (final) dislocation centre. Thin solid lines indicate the three $\{110\}$ planes in (c), and the three $\{112\}$ planes in (h). Thick (green) arrows represent the moving direction of the dislocation core. (For interpretation of the references to colour in this figure legend, the reader is referred to the web version of this article.)

investigated by using the first-principles total energy method based on the density functional theory. An ideal defective system containing only one defect (a point defect) has been characterized and determined as the maximum tensile stress required to reach elastic instability under increasing load. This can be regarded as the intrinsic local strength of a defect region in real materials. Computational tensile tests on a single W crystal with and without defects have been performed by using the CPMD (Car Parrinello Molecular Dynamics) code [64]. We employed Goedecker–Teter–Hutter pseudopotentials with generalized gradient approximation [65,66]. The electronic wave functions are expended in a plane-wave basis set with a kinetic energy cut-off equal to 80 Ry. The latter value has been chosen by preliminary calculations on each element of the alloys. All the calculations are performed in the supercell approximation with periodic boundary conditions meant to mimic an infinitely extended system. A cubic supercell $3 \times 3 \times 3$ (54 atoms) has been considered. The role of the point defects in W bulk is investigated by replacing a W atom with Re, Ta and V atoms. The validity of the numerical model has been extensively checked by computing several structural properties of pure W and its alloys. We have calculated lattice constants, bulk modulus, enthalpies of atomization and formation enthalpy of defects in very good agreement with experimental results. In the first-principles computational tensile test, a uniaxial tensile strain is applied to the chosen crystalline direction of bcc W and bcc W alloys. After the calculation of the total energy of the unloaded material, the crystal has been elongated along the loading axis (the [0 0 1] direction) by a fixed amount ε, which is equivalent to applying some tensile stress σ. To ensure uniaxial loading, the dimensions of the crystal in directions perpendicular to the loading axis have been relaxed by finding the minimum of the total energy as a function of these dimensions. Then, at each strain step, the structure has been fully relaxed until all the other five components of the stress vanish except that in the tensile direction. We have thus obtained the total energy E as a function of the strain ε.

For the uniaxial tensile strain, the tensile stress σ is calculated from

$$\sigma = \frac{1}{\Omega(\varepsilon)} \frac{\partial E}{\partial \varepsilon}$$

where E is the total energy and Ω is the volume at a given tensile strain of ε. The tensile stress for each strain step has been calculated, and thus the stress–strain relation and the ideal tensile strength has been obtained. This approach has been applied for bcc W and for bcc W alloys, to obtain total energy–strain relations, stress–strain relations and the ideal tensile strengths. Despite the low concentration of defects (less than 2%), the results highlight that the presence of substitutional defects in W bulk is able to produce measurable variations with respect to pure tungsten crystal. The bulk modulus decreases for all the W alloys. The ideal tensile strength in the [0 0 1] direction decreases in the presence of Re or Ta, and it increases in W–V alloy. However, additional investigations on structural and mechanical properties of W in the presence of higher concentration of defects are in progress.

A rate equation simulation (RE) method was developed for hydrogen implantation into W, where all the defect concentrations, intrinsic and irradiation-induced ones, are solved together with the hydrogen present in the sample. The numerous material parameters for the RE were taken from the literature [67–69]. For validating the RE code, an exemplary system of 5, 15 and 30 keV deuterium (D) implantation into W was analyzed with the RE method and the results were compared with corresponding experimental results [70]. The implantation time, dose and temperature used in the RE simulations were taken from the experimental set-up. The primary D–W irradiation-induced collision statistics were
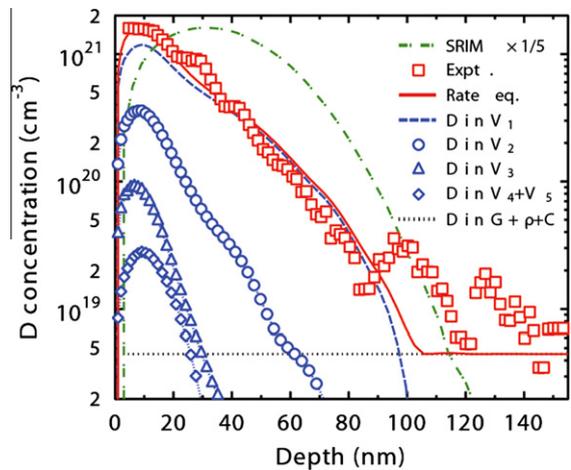

Fig. 25. Results for the experimental 5 keV/D implantation and corresponding rate equation simulations. The total simulated D profile (solid line) consists mainly of D trapped in monovacancies, while the concentration of D trapped in larger vacancy clusters decreases along with the cluster size. G is grain boundary, ρ dislocation and C is carbon impurity. The SRIM simulation shows the D profile if the implantation is done at a temperature where D is immobile.

determined by binary collision approximation calculations with SRIM and the W collision cascades by Molecular Dynamics (MD) [69] simulations. The activation energies needed for detrapping of D from the resulted irradiation-induced trap sites were determined with first-principles calculations using electron density functional theory (DFT) [68]. A full, detailed description of the present RE method and its inputs from MD and DFT calculations have been published recently [71].

The validated RE code is suitable for simulating hydrogen implantations into W with fluences below the blistering threshold. Fig. 25 presents the 5 keV/D implantation RE result compared with the experimental D concentration. An excellent agreement can be seen with the RE simulated and experimentally obtained D profile. According to RE, over 90% of the retained D is trapped at
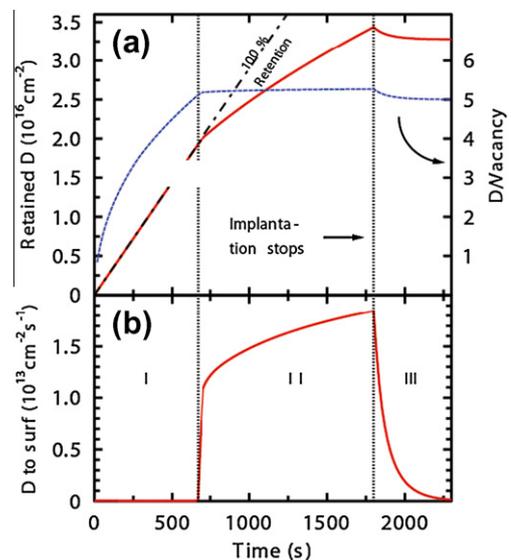

Fig. 26. Retention and recycling of D during implantation as simulated with RE. (a) Retained D and the mean number of D trapped per vacancy during and after 30 keV/D RT implantation. (b) The flux of D atoms from bulk to sample surface. Region I: Vacancies are slowly filling up with D, 100% retention. Region II: Vacancies are saturated with D, and D flux to surface starts. Region III: Weakly bound sixth D detraps from vacancies after the implantation.

mono-vacancies (V1) after the implantation. Fig. 26a presents the amount of D retention in the sample during and after 30 keV/D implantation. In the figure, three distinct regions are seen. In region I, the retained D is the same as the implanted one (100% retention, backscattered fraction excluded). In region II, the vacancies become saturated with D and the mean number of trapped D per vacancy is between five and six. All implanted D atoms are no longer trapped and part of D diffuses deeper into the sample and to the sample surface. Fig. 26b shows the simultaneous onset of D atom flux to the W surface. After the implantation has stopped (region III), the D retention drops and a remnant D flux to the W surface takes place for about 10 min. The simulation shows that directly after the implantation, the solute D concentration decreases rapidly to zero. The slow decrease in retained D is the detrapping of the sixth D from the vacancies (trapping energy 0.61 eV). This post-implantation effect has been seen experimentally, for example, by Garcia-Rosales et al. [72] and Pisarev et al. [73], where the observed D_2 desorption from the sample surface resembles the present simulated D flux to surface.

The formation of voids in 800 keV ^{3}He implanted tungsten further annealed has been modelled using an object kinetic Monte Carlo (OKMC) code [74]. These simulations underline the role of the He atoms in the track region (700 nm from the surface), which, despite their small number, act as germs for the formation of nanovoids [75]. The parameterization of the code is based on first principles calculations [74]. The implanted ions flux is modelled using cascade debris calculated by Marlowe (a code based on binary collision approximation) [76]. This work includes experimental investigations on the nanovoid formation using Positron Annihilation Spectroscopy [77] and the simulation conditions have been chosen to model these experiments. Different fluences (implanted at 300 K) have been investigated ranging from 10^{13} to 5×10^{16} ions cm^{-2}. Fig. 27a gives the mono-vacancy concentration at the end of the implantation. Good agreement with the experimental results has been obtained because the model takes into account the diffusion of Self Interstitial Atoms (SIAs) and He atoms which takes place at the implantation temperature (300 K), and the resulting amount of recombinations. The isochronal annealing sequences start at 300 K up to 900 K. A good agreement with the experimental observations has been obtained concerning the clustering temperature ranges (occurring when the vacancies start to diffuse and form clusters). Fig. 27b gives the concentration of pure vacancy and mixed He-vacancy clusters versus the number of vacancies in the clusters at 900 K for 3 of the investigated fluences. The clusters contain on average from 100 to 20 vacancies when the fluence increases. Despite its simplicity, the OKMC model agrees

with the experimentally estimated number of vacancies in the nanovoids (above 30 vacancies). Furthermore, as observed experimentally, the number of vacancies in the nanovoids decreases when the fluence increases. The role of the He atoms is underlined by the large amount of He-vacancy clusters as compared with the number of pure vacancy clusters. Furthermore, it was shown that without the He atoms, the trends in the evolution of the nanovoid size versus fluence are not reproduced.

The migration of small He clusters and the influence of impurities have been investigated using Density Functional calculations and the VASP code. The results indicate that small He clusters are mobile. Furthermore, it was found that 2He clusters have a 1D motion along the ⟨1 1 1⟩ direction at low temperatures (150–600 K). When the temperature increases, the 2He cluster can change ⟨1 1 1⟩ direction, and the higher the temperature, the more the motion varies in three dimensions (see Fig. 28). The binding energies of selected impurities with He and small He clusters were determined. It was seen that most of the investigated substitutional impurities can trap He atoms as well as small He clusters. The exception is Re, and we anticipate thus that the introduction of Re, either to improve the mechanical properties or because of transmutation, will not affect He transport in W.

Furthermore, the recent DFT predictions appear consistent with experimental observations showing that W–Ta and W–V alloys are brittle (they are even more brittle than pure tungsten). Ab-initio based simulations of the phase stability of tungsten–tantalum (W–Ta) and tungsten–vanadium (W–V) binary alloys were performed in [78,79]. In these references, the phase stability of W–V and W–Ta alloys was investigated using first-principles quantum–mechanical electronic structure based calculations, combined with cluster expansion Monte-Carlo simulations. The calculations predicted the formation of a number of inter-metallic phases, all characterized by a negative enthalpy of formation, with the lowest enthalpy of mixing found for the W2V and W5Ta3 compounds. The prediction of these complex phases and the fact that they are still present at high temperatures is consistent with the results of Charpy impact tests performed on W–5%Ta and W–5%V alloys showing that, compared to pure tungsten, the ductile-to-brittle transition temperatures (DBTT) of all the W–V and W–Ta alloys are higher than that of pure W, i.e. they are more brittle than tungsten. The formation of intermetallic compounds in tungsten alloys is just one of the factors responsible for their increased hardening, the other being the conventional solute hardening that gives rise to the embrittlement of the alloys that occurs even in the limit where the concentration of the alloying elements is small. Fig. 29 illustrates some of the findings derived from first-principles calculations. It shows that
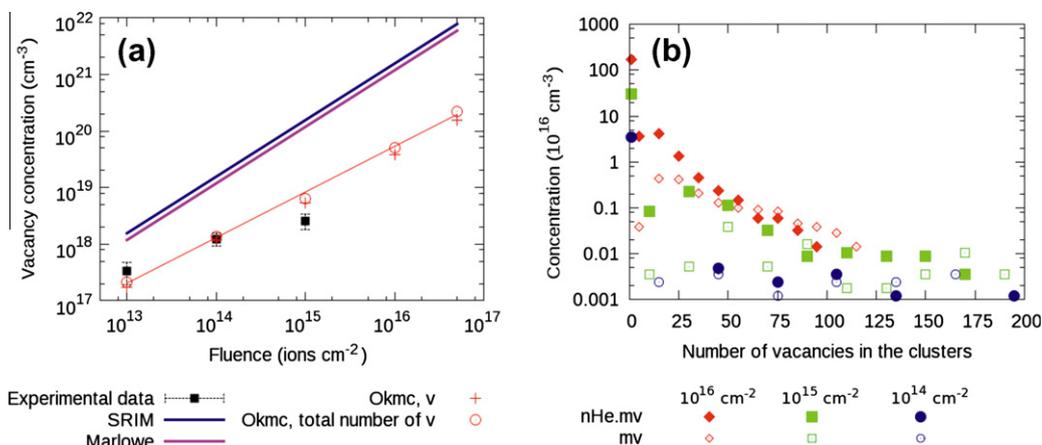

Fig. 27. (a) Comparison of the experimentally measured mono-vacancy concentration and the concentrations of vacancies calculated with SRIM, Marlowe and the Okmc model). (b) Mixed (nHe.mv) and pure (mv) cluster concentrations versus the number of vacancies in the clusters at 900 K for the three different fluences.
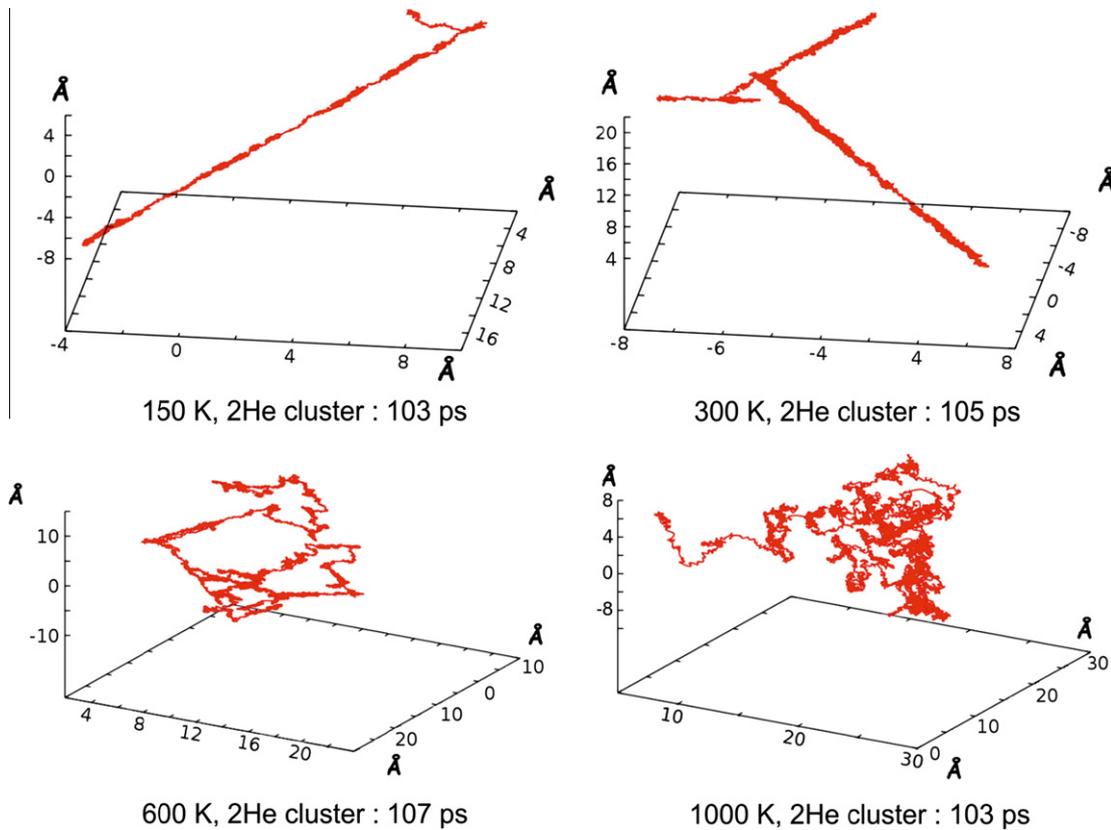
Fig. 28. Centre of mass trajectory of a 2He cluster at 150 K, 300 K, 600 K and 1000 K. The axes (x,y,z) are parallel to the $\langle 100 \rangle$, $\langle 010 \rangle$, and $\langle 001 \rangle$ direction of the crystal lattice.
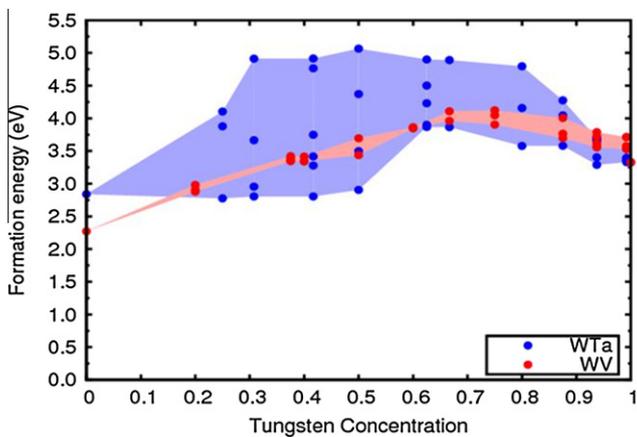

Fig. 29. Vacancy formation energies for tungsten–tantalum and tungsten–vanadium alloys delivered from density functional theory (DFT) calculations.

the vacancy formation energy in W–Ta alloys depends strongly on the lattice site at which a vacancy is formed, whereas in W–V alloys it is almost independent of the location of the vacancy site. The results show the possibility of designing alloys where vacancies form within a desired range of temperature, suggesting the possibility of developing alloys with improved stability under irradiation. Therefore, the programme continues with its previous strategy to evaluate new tungsten materials for both applications (structural and armour) prior to a final assessment.

Materials bombarded by neutrons from a fusion plasma will undergo non-elastic nuclear reactions, whose cross-section ('reaction probability') is strongly dependent on the incident neutron energy. Using the neutron fluxes and energy-spectra predicted by a neutron-transport code (MCNP), inventory calculations provide quantitative estimates of the concentrations of impurities generated – transmutation products. In W, the production of impurities, such as Re, Ta, and Os, is fairly significant, being of the order of a few thousand to tens of thousands of atomic parts per million (appm) over a typical DEMO-like first-wall 5-year neutron exposure. Over such a timescale, this leads to W falling from 100 atomic % initially, to less than 94 at.%. Under the same conditions, other materials, by comparison, would hardly be transmuted (burnt-up) at all; for instance, in pure Fe, the total concentration of all transmutation products after 5 years is only around 1 at.%. Thus, it is conceivable that components constructed of W, with its relatively high transmutation rates, would experience measurable changes in mechanical and structural properties. Perhaps the only good news as far as W is concerned is that helium is generated in relatively modest quantities, typically only reaching a few tens of appm over the expected normal lifetime of first wall fusion-reactor components. However, several of the materials under discussion for W-alloys, such as Ti and V, produce an order of magnitude more He compared to W (or Re or Ta), and so the actual ability of W and W-alloys to withstand the effects of the embrittlement mechanisms activated by He must be carefully considered [80].

6. Summary and outlook

The long-term goal of the EFDA programme on divertor materials is to provide structural and functional materials together with the necessary production and fabrication technology for future fusion reactors beyond ITER. While fabrication issues are far advanced and well investigated, the most critical part of the programme is still the development of a material for structural

divertor parts. So far, thin tungsten plates show the best ductility, as long as specific fabrication or machine rules are followed: (1) stress concentrators have to be avoided and (2) the anisotropic microstructure has to be aligned to the contour of the according part. Joining of tungsten materials is possible, but design routes, cost and low-activation criteria probably have to be redefined for brazing materials. The simulation of possible armour materials is well established by the use of the JUDITH and GLADIS facilities. The results clearly show that the calculated sputtering rates might be far too low compared to the real in-service conditions. A complete picture of the irradiation performance of tungsten materials is not yet available. But for further, more specific designs at least, basic irradiation damage data have to be produced. This, together with the aforementioned issues, should be at the top of the priority list of fusion material programmes in general.

Acknowledgements

References

[1] J. Pamela, A. Bécoulet, D. Borba, J.-L. Boutard, L. Horton, D. Maisonnier, Fusion Eng. Des. 84 (2009) 194–204.
[2] D. Maisonnier, D. Campbell, I. Cook, L. Di Pace, L. Giancarli, J. Hayward, A. Li Puma, M. Medrano, P. Norajitra, M. Roccella, P. Sardain, M.Q. Tran, D. Ward, Nucl. Fusion 47 (2007) 1524–1532.
[3] P. Norajitra, S.I. Abdel-Khalik, L.M. Giancarli, T. Ihli, G. Janeschitz, S. Malang, I.V. Mazul, P. Sardain, Fusion Eng. Des. 83 (2008) 893–902.
[4] G. Janeschitz, J. Nucl. Mater. 290–293 (2001) 1.
[5] H. Bolt, V. Barabash, G. Federici, J. Linke, A. Loarte, J. Roth, K. Sato, J. Nucl. Mater. 307–311 (2002) 43.
[6] K. Wittlich, T. Hirai, J. Compan, N. Klimov, J. Linke, A. Loarte, M. Merola, G. Pintsuk, V. Podkovyrov, L. Singheiser, A. Zhitlukhin, Fusion Eng. Des. 84 (2009) 1982.
[7] T. Hirai, G. Pintsuk, J. Linke, M. Batilliot, J. Nucl. Mater. 390–391 (2009) 751.
[8] J. Roth, E. Tsitrone, A. Loarte, Th. Loarer, G. Counsell, R. Neu, V. Philipps, S. Brezinsek, M. Lehnen, P. Coad, Ch. Grisolia, K. Schmid, K. Krieger, A. Kallenbach, B. Lipschultz, R. Doerner, R. Causey, V. Alimov, W. Shu, O. Ogorodnikova, A. Kirschner, G. Federici, A. Kukushkin, and EFDA PWI Task Force, ITER PWI Team, Fusion for Energy, ITPA SOL/DIV, J. Nucl. Mater. 390–391 (2009) 1.
[9] M. Rieth, J.L. Boutard, S.L. Dudarev, T. Ahlgren, S. Antusch, N. Baluc, M.-F. Barthe, C.S. Becquart, L. Ciupinski, J.B. Correia, C. Domain, J. Fikar, E. Fortuna, C.-C. Fu, E. Gaganidze, T.L. Galán, C. García-Rosales, B. Gludovatz, H. Greuner, K. Heinola, N. Holstein, N. Juslin, F. Koch, W. Krauss, K.J. Kurzydlowski, J. Linke, Ch. Linsmeier, N. Luzginova, H. Maier, M.S. Martínez, J.M. Missiaen, M. Muhammed, A. Muñoz, M. Muzyk, K. Nordlund, D. Nguyen-Manh, P. Norajitra, J. Opschoor, G. Pintsuk, R. Pippan, G. Ritz, L. Romaner, D. Rupp, R. Schäublin, J. Schlosser, I. Uytdenhouwen, J.G. van der Laan, L. Veleva, L. Ventelon, S. Wahlberg, F. Willaime, S. Wurster, M.A. Yar, J. Nucl. Mater. 417 (2011) 463.
[10] J. Reiser, M. Rieth, B. Dafferner, S. Baumgärtner, R. Ziegler, A. Hoffmann, Fusion Eng. Des. (2011), http://dx.doi.org/10.1016/j.fusengdes.2011.07.011.
[11] S. Antusch, P. Norajitra, V. Piotter, H.-J. Ritzhaupt-Kleissl, L. Spatafora, Fusion Eng. Des. 86 (2011) 1575–1578.
[12] T. Weber, J. Aktaa, Fusion Eng. Des. 86 (2011) 220–226.
[13] T. Weber, M. Härtelt, J. Aktaa, Eng. Fract. Mech., in press.
[14] J. Matějíček, H. Boldyryeva, V. Brožek, E. Cižmárová, Z. Pala, in: Tungsten-Steel Composites and FGMs Produced by Hot Pressing; Proc. 21st International Conference on Metallurgy and Materials METAL 2012, Brno 2012, paper no. 177.
[15] J. Matějíček, P. Chráska, J. Linke, J. Thermal Spray Technol. 16 (2007) 64–83.
[16] J. Matejicek, V. Weinzettl, E. Dufkova, V. Piffl, V. Perina, ActaTechnica CSAV 51 (2) (2006) 179–191.
[17] H. Greuner, H. Bolt, B. Böswirth, S. Lindig, W. Kühnlein, T. Huber, K. Sato, S. Suzuki, Fusion Eng. Des. 75–79 (2005) 333–338.
[18] T. Kavka, J. Matejíček, P. Ctibor, M. Hrabovský, J. Thermal Spray Technol. 21 (3–4) (2012) 695–705.
[19] Z. Zhong, T. Hinoki, T. Nozawa, Y-H. Park, A. Kohyama, J. Alloys Compd. 489 (2010) 545–551.
[20] M. Rosinski, M.J. Kruszewski, A. Michalski, E. Fortuna-Zalesna, L. Ciupinski, K.J. Kurzydlowski, Fusion Eng. Des. 86 (2011) 2573.
[21] M. Rieth, A. Hoffmann, Int. J. Refract. Met. Hard Mater. 28 (2010) 679.
[22] A. Luo, D.L. Jacobson, K.S. Shin, Refract. Met. Hard Mater. 10 (1991) 107–114.
[23] A. Giannattasio, S.G. Roberts, Philos. Mag. 87 (2007) 2589.
[24] A. Giannattasio, Z. Yao, E. Tarleton, S.G. Roberts, Philos. Mag. 90 (2010) 3947.
[25] J.D. Murphy, A. Giannattasio, Z. Yao, C.J.D. Hetherington, P.D. Nellist, S.G. Roberts, J. Nucl. Mater. 386–88 (2009) 583.
[26] D. Di Maio, S.G. Roberts, J. Mater. Res. 20 (2005) 299.
[27] D.E.J. Armstrong, M.E. Rogers, S.G. Roberts, Scripta Mater. 61 (2009) 741.
[28] D.E.J. Armstrong, A.J. Wilkinson, S.G. Roberts, Philos. Mag. Lett. 91 (2011) 394.
[29] L.Veleva, Contribution to the production and characterization of W–Y, W–Y$_2$O$_3$ and W–TiC Materials for Fusion Reactors, Thesis EPFL No. 4995, 2011.
[30] M. Battabyal, R. Schäublin, P. Spätig, M. Walter, M. Rieth, N. Baluc, Microstructure and mechanical properties of a W–2 wt.%Y$_2$O$_3$ composite produced by sintering and hot forging, J. Nuc. Mater., submitted for publication.
[31] M.A. Yar, S. Wahlberg, H. Bergqvist, H.G. Salem, M. Johansson, M. Muhammed, J. Nucl. Mater. 408 (2011) 129.
[32] J. Du, T. Höschen, M. Rasinski, S. Wurster, W. Grosinger, J.H. You, Compos. Sci. Technol. 70 (2010) 1482–1489.
[33] J. Du, T. Höschen, M. Rasinski, J.H. You, J. Nucl. Mater. 417 (2011) 472–476.
[34] J. Du, T. Höschen, M. Rasinski, J.H. You, Mater. Sci. Eng. A 527 (2010) 1623–1629.
[35] J. Riesch, T. Höschen, A. Galatanu, J.H. You, Tungsten-fibre reinforced tungsten composites: a novel concept for improving the toughness of tungsten, in: Proceedings of 18th International Conference on Composite Materials (ICCM18), 2011-08-22–2011-08-26 Jeju Island, Korea.
[36] A.G. Evans, Acta Materialia 45 (1) (1997) S. 23–S. 40.
[37] J. Riesch, C. Linsmeier, S.F. Nielsen, In-situ tomographic observation of crack formation and propagation in tungsten materials in the framework of FEMaS-CA (part of: Challenges in materials sciences and possibilities in 3D and 4D characterization techniques), in: Proceedings, vol. 512, 2010 Danmarks Tekniske Universitet, Riso Nationallaboratoriet for Baeredygtig Energi, Roskilde, pp. 405–412. ISBN: 978-87-550-3833-2.
[38] V. Livramento, D. Nunes, J.B. Correia, P.A. Carvalho, R. Mateus, K. Hanada, N. Shohoji, H. Fernandes, C. Silva, E. Alves, Tungsten–tantalum composites for plasma facing components, in: Materials for Energy 2010, ENMAT2010, 4–8 July 2010, Karlsruhe, Germany.
[39] E. Gaganidze, D. Rupp, Fracture behavior of anisotropic polycrystalline tungsten, J. Nucl. Mater., in preparation.
[40] D. Rupp, S.M. Weygand, Philos. Mag. 90 (2010) 4055–4069.
[41] R. Duwe, W. Kühnlein, M. Münstermann, Proc. 18th SOFT, Karlsruhe, Germany, 1994, Fusion Technology, 1994, p. 335.
[42] H. Greuner, H. Bolt, B. Böswirth, S. Lindig, W. Kuhnlein, T. Huber, K. Sato, S. Suzuki, Fusion Eng. Des. 75 (2005) 333.
[43] D. Maisonnier et al., A Conceptual Study of Commercial Fusion Power Plants, Final Report, EFDA-RP-RE-5.0, 13 April 2005.
[44] F. Koch, H. Bolt, Phys. Scr. T128 (2007) 100–105.
[45] F. Koch, S. Köppl, H. Bolt, J. Nucl. Mater. 386–388 (2009) 572–574.
[46] F. Koch, J. Brinkmann, S. Lindig, T.P. Mishra, Ch. Linsmeier, Oxidation behaviour of silicon-free tungsten alloys for use as first wall material, Phys. Scr. T145 (2011) 014019.
[47] P. López-Ruiz, N. Ordás, S. Lindig, F. Koch, I. Iturriza, C. García-Rosales, Self-passivating bulk tungsten-based alloys manufactured by powder metallurgy, Phys. Scr. T145 (2011) 014018.
[48] P. López-Ruiz, N. Ordás, I. Iturriza, F. Koch and C. García-Rosales, Powder metallurgical processing of self-passivating tungsten alloys for fusion first wall application, J. Nucl. Mater. (2012), accepted for publication.
[49] F. Koch, U. Auzmendi, J. Brinkmann, P. López-Ruiz, N. Ordás, S. Lindig, M. Balden, C. García-Rosales, Ch. Linsmeier, private communication.
[50] T. Weitkamp, P. Tafforeau, E. Boller, P. Cloetens, J.-P. Valade, P. Bernard, F. Peyrin, W. Ludwig, L. Helfen, J. Baruchel, AIP Conf. Proc. 1221 (2010) 33–38.
[51] A. Zivelonghi, T. Weitkamp, M. Rasinski, G. Waizmann, Preliminary Study of Microtomography on Plasma-Sprayed Tungsten, ESRF User report, Experiment MA-890, September 2009. <http://ftp.esrf.eu/pub/UserReports/42915_A.pdf>.
[52] A. Zivelonghi, Thermomechanical Behaviour of Two Heterogeneous Tungsten Materials via 2D and 3D Image-Based FEM, PhD Thesis, Technische Universität München, 2011.
[53] H. Bolt, V. Barabash, W. Krauss, et al., J. Nucl. Mater. 329–333 (2004) 66–73.
[54] H. Greuner, H. Bolt, B. Böswirth, S. Lindig, W. Kühnlein, T. Huber, Fusion Eng. Des. 75–79 (2005) 333.
[55] B. Gludovatz, S. Wurster, T. Weingärtner, A. Hoffmann, R. Pippan, Philos. Mag. 91 (2011) 3006–3020.
[56] D. Rupp, S.M. Weygand, Philos. Mag. 90 (2010) 4055–4069.
[57] S. Wurster, B. Gludovatz, A. Hoffmann, R. Pippan, J. Nucl. Mater. 413 (2011) 166–176.
[58] B. Gludovatz, S. Wurster, A. Hoffmann, R. Pippan, Influence of deformation, microstructure and temperature on the fracture resistance of tungsten, in preparation.
[59] B. Gludovatz, S. Wurster, A. Hoffmann, R. Pippan, A study into the crack propagation resistance of pure tungsten, Eng. Fract. Mech., (2012), http://dx.doi.org/10.1016/j.engfracmech.2012.07.021.
[60] V. Vitek, Philos. Mag. 84 (2004) 415.
[61] L. Ventelon, F. Willaime, P. Leyronnas, J. Nucl. Mater. 26 (2009) 386.
[62] L. Romaner, C. Ambrosch-Draxl, R. Pippan, Phys. Rev. Lett. 104 (2010) 195503.
[63] H. Li, S. Wurster, C. Motz, L. Romaner, C. Ambrosch-Draxl, R. Pippan, Acta Mater. 60 (2012) 748.
[64] CPMD, Copyright IBM Corp 1990–2008. Copyright MPI für Festkörperforschung Stuttgart 1997-2001. <http://www.cpmd.org>.
[65] S. Goedecker, M. Teter, J. Hutter, Phys. Rev. B 54 (1996) 1703.
[66] C. Hartwigsen, S. Goedecker, J. Hutter, Phys. Rev. B 58 (1998) 3641.

[67] K. Heinola, T. Ahlgren, J. Appl. Phys. 107 (2010) 113531.
[68] K. Heinola, T. Ahlgren, K. Nordlund, J. Keinonen, Phys. Rev. B. 82 (2010) 094102.
[69] T. Ahlgren, K. Heinola, N. Juslin, A. Kuronen, J. Appl. Phys. 107 (2010) 033516.
[70] K. Heinola, T. Ahlgren, E. Vainonen-Ahlgren, J. Likonen, J. Keinonen, Phys. Scripta T128 (2007) 91.
[71] T. Ahlgren, K. Heinola, K. Vörtler, J. Keinonen, J. Nucl. Mater. 427 (2012) 152.
[72] C. Garcıa-Rosales, P. Franzen, H. Plank, J. Roth, E. Gauthier, J. Nucl. Mater. 233–237 (1996) 803.
[73] A.A. Pisarev, I.D. Voskresensky, S.I.J. Porfirev, J. Nucl. Mater. 313–316 (2003) 604.

[74] C.S. Becquart, C. Domain, U. Sarkar, A. Debacker, M. Hou, J. Nucl. Mater. 403 (2010) 75.
[75] A. Debacker, C.S. Becquart, M.F. Barthe, P.E. Lhuillier, J. Nucl. Mater. 429 (2012) 78.
[76] M. Hou, C. Ortiz, C.S. Becquart, C. Domain, U. Sarkar, A. Debacker, J. Nucl. Mater. 403 (2010) 89.
[77] A. Debelle, M.F. Barthe, T. Sauvage, J. Nucl. Mater. 376 (2) (2008) 216.
[78] D. Nguyen-Manh, M. Muzyk, K.J. Kurzydlowski, N.L. Baluc, M. Rieth, S.L. Dudarev, Key Eng. Mater. 465 (2011) 15–20.
[79] M. Muzyk, D. Nguyen-Manh, K.J. Kurzydłowski, N.L. Baluc, S.L. Dudarev, Phys. Rev. B 84 (2011) 104115.
[80] M.R. Gilbert, J.-Ch. Sublet, Nucl. Fusion 51 (2011) 043005.